applied sciences

MDPI

Article

Effects and Mechanisms of Injection Strategies on NH_3/CH_4 Swirl Co-Firing and Emission Characteristics

Bing Kang [1,2], Youxing Wei [1,3,4,*], Peisheng Li [1,3,4], Fei Deng [1,3,4], Yong Wang [1], Xiangbing Zou [1], Xiao Qiu [1] and Chenyang Liao [1]

[1] School of Electrical Engineering, Jiangxi University of Water Resources and Electric Power, Nanchang 330099, China; kangbing@juwp.edu.cn (B.K.); 17879601446@163.com (Y.W.); 18770531314@163.com (X.Z.); qx3163589163@163.com (X.Q.); 15279087767@163.com (C.L.)
[2] Jiangxi Engineering Center for High-Power Electronics and Intelligent Grid Metrology, Nanchang 330099, China
[3] Key Laboratory of Energy Low-Carbon Conversion and Storage, Jiangxi Provincial Department of Education, Nanchang 330099, China
[4] Nanchang Key Laboratory of Low Grade Energy Conversion and Systematic Energy Saving Technology, Nanchang 330099, China
* Correspondence: youxingwei@juwp.edu.cn

Abstract

Developing green ammonia (NH_3) as a carbon-free fuel faces challenges of flame instability and high NO_x emissions, requiring optimized strategies for aerodynamic flow and fuel-air mixing. This study investigates four combustion organization modes, combining primary air routing (axial/tangential) and fuel-air mixing states (premixed/non-premixed) using a swirl burner. Experiments were conducted under lean conditions ($\varphi = 0.9$) across NH_3 blending ratios (0~100%), alongside chemical reactor network (CRN) modeling. Increasing NH_3 transitions flame topology from V-shape to M-shape, ultimately resulting in flame lift-off. Tangential injection broadens stability limits via strong shear vortices (sustaining combustion at 90%NH_3), while its non-premixed mode reduces peak CO emissions by 36.5% versus the axial premixed baseline, and the peak weighted combined emission index (iCO + jNO) is reduced by approximately 18% on average. A favorable synergistic emission trade-off window of C-N exists around 17%NH_3 based on iCO + jNO. CRN modeling confirms that the $NH_2 \rightarrow HNO \rightarrow NO$ pathway constitutes the primary backbone for nitrogen migration. At 30%NH_3, increased $HNO + H \rightarrow H_2 + NO$ reaction rates cause a rapid increase in fuel-NO_x. Conversely, the non-premixed strategy creates local fuel-rich reduction zones at 70%NH_3. Based on CRN kinetic inferences, these zones promote amine radical fluxes that effectively lead to a significant reduction in measured NO. These findings provide theoretical support and baseline data for optimizing low- or zero-carbon NH_3 swirl burners on a certain scale.

Keywords: NH_3/CH_4 co-firing; swirl flame; injection strategy; NO emissions; CRN

Check for updates

Academic Editor: Jun Cong Ge

Received: 19 September 2026
Revised: 16 October 2026
Accepted: 22 October 2026
Published: 3 November 2026

Copyright: © 2026 by the authors. Licensee MDPI, Basel, Switzerland. This article is an open access article distributed under the terms and conditions of the Creative Commons Attribution (CC BY) license.

1. Introduction

The urgent demand for global climate mitigation and carbon neutrality has accelerated the development of next-generation power systems centered on carbon-free energy carriers [1,2]. Although hydrogen is widely regarded as a prime candidate for decarbonizing the energy sector, its large-scale application is currently constrained by inherent technical bottlenecks, including low volumetric energy density, high storage pressures, and the risk of hydrogen embrittlement during transportation [3–5]. In this context, green NH_3 has

emerged as a highly promising alternative carbon-free fuel. Due to its high hydrogen content (17.6 wt.%), NH_3 serves as an efficient hydrogen carrier. Moreover, it liquefies under mild conditions (25 °C and 0.8 MPa), allowing it to leverage existing global industrial synthesis, storage, and distribution infrastructure [6,7]. Recent advancements in NH_3 combustion technologies have validated its feasibility in internal combustion engines [8,9], industrial boilers [10,11], and gas turbines [12,13], demonstrating its substantial potential to reduce carbon footprints in the power and thermal industries. However, the practical application of pure NH_3 as a fuel still faces severe challenges, namely combustion instability and high nitrogen oxide (NO_x) emissions [14]. The former stems from the high autoignition temperature (650 °C), low laminar burning velocity (≈7 cm/s), and narrow flammability limits of NH_3, while the latter is due to the high propensity for NO_x formation via oxidation of fuel-bound nitrogen.

To overcome the poor ignition performance and flame instability of NH_3, researchers have extensively explored various enhancement strategies. These methods include oxy-fuel combustion [15,16], NH_3 pre-heating and cracking for hydrogen production [17,18], and plasma-assisted combustion [19,20]. Among these approaches, blending NH_3 with high-reactivity fuels remains one of the most economically and technically viable solutions at present. Methane (CH_4) is the primary component of natural gas, which is frequently used as a supplementary fuel in gas turbines and gas-fired boilers to enhance NH_3 combustion intensity [21]. Previous studies have shown that in a fully premixed NH_3/CH_4/air flat flame with 60% methane (molar fraction, corresponding to an NH_3 energy share of $E_{NH3} = 0.21$), the laminar burning velocity can be increased to more than three times that of a pure NH_3/air flame [22]. Furthermore, co-firing with 50 vol.% CH_4 ($E_{NH3} = 0.28$) widens the lean/rich flammability limits from $\varphi = 0.79$~1.24 (for pure NH_3/air flames) to $\varphi = 0.61$~1.40 [23]. By quantifying the fundamental laminar burning velocities of NH_3/CH_4 mixtures, researchers further revealed that adding CH_4 enriches the radical pool (e.g., OH, H, and O), thereby accelerating the overall reaction rate [24]. Xiao et al. [25] numerically analyzed NH_3/CH_4 co-firing under realistic gas turbine combustor conditions to explore the industrial feasibility of blended combustion. Kurata et al. [26] investigated the operational characteristics of an NH_3/CH_4 gas turbine power generation system under varying power outputs, confirming that mixing CH_4 can effectively compensate for the low combustion intensity of NH_3, thereby improving the flame stability of gas turbine burners. Evidently, the addition of CH_4 significantly enhances the flame propagation speed of NH_3 and broadens its stable operating range. Despite these advancements, introducing carbon-containing fuels into NH_3 systems complicates chemical kinetic pathways, often leading to a trade-off between carbon reduction and NO_x emission control, underscoring the urgent need to optimize the combustion organization process.

In NH_3/CH_4 co-firing systems, even a minor ammonia mole fraction of 22% ($E_{NH3} = 0.10$) can cause flue gas NO concentrations to surge into the range of 10^3~10^4 ppm. This is several orders of magnitude higher than that of pure CH_4 combustion and far exceeds acceptable engineering limits [27]. From kinetic and mechanistic perspectives, the conversion of fuel-N to NO_x is strongly influenced by local temperatures, key radical concentrations (e.g., NH_i, H, O, OH), local equivalence ratios (premixed or non-premixed states), and the aerodynamic history of fluid parcels [28,29]. Consequently, in addition to adding reactive fuels, the spatial organization and control of combustion injection play a decisive role in suppressing NO_x emissions. Moreover, spatial non-uniformity introduces opportunities for more sophisticated combustion designs and control techniques. Leveraging the inherent capability of NH_3 to reduce NO, multi-stage combustion (fuel/air staging) can sequentially establish fuel-rich, quenching, and fuel-lean atmospheres, thereby providing abundant NH_i radicals to promote NO reduction [30]. However, research indicates [31,32] that

conventional premixed swirl NH_3/CH_4/air flames can only restrict NO emissions below 3000 ppm under highly fuel-rich conditions ($\varphi > 1.1$). Furthermore, CRN analyses have indicated that introducing secondary air into air-staged combustion of NH_3/CH_4 mixtures may cause secondary oxidation of unreacted NH_3 from the fuel-rich zone, leading to an unwanted increase in total NO yield [33].

In this context, breaking through the CO-NO_x synergistic control dilemma while ensuring flame stability during co-firing has become a current hot research topic. Swirl combustion is widely adopted in industrial burners and gas turbines due to its ability to generate a central toroidal recirculation zone (CTRZ) and to provide a continuous ignition source at the burner exit [34,35]. Hayakawa et al. [36] investigated the effects of burner configuration on flame stability and emission characteristics at ambient temperature and pressure, confirming the configuration's effectiveness in stabilizing NH_3 flames. However, the intense interaction between the swirl field and NH_3/CH_4 chemical kinetics renders the emission performance highly sensitive to specific injection strategies. To this end, researchers have begun exploring differentiated fuel-air mixing strategies. Valera-Medina et al. [5] utilized a tangential swirl burner to evaluate the flame stability and emissions of NH_3/CH_4 blended fuels under various equivalence ratios. Their results indicated that under lean conditions, non-premixed flames exhibit a lower propensity to form NO than premixed flames. These findings across various configurations suggest that modulating the fuel-air injection and mixing modes is crucial for controlling NO_x. However, it remains unclear which spatial flow organization and injection strategy (denoting the spatial combination of aerodynamic inlet routing, i.e., axial/tangential, and fuel-air mixing state, i.e., premixed/non-premixed) is the most effective. In recent years, substantial progress has been made in understanding turbulent NH_3 swirl combustion, particularly for NH_3/CH_4 and NH_3/biogas blends [37,38]. Recent studies demonstrate that elevating the NH_3 fraction not only alters flame strain rates but also increases the progress variable variance across the flame front, which fundamentally modulates turbulent flame speed and enhances localized flame-holding stability under intense swirl conditions. Specifically, Yang et al. [21] demonstrated that injecting ammonia centrally into a swirling methane atmosphere creates local fuel-rich pockets that enrich NH_2 radicals, thereby significantly promoting NH_2-mediated NO reduction pathways. Similarly, Wang et al. [39] confirmed that controlled fuel stratification under partially premixed swirling modes effectively alters nitrogen kinetics and achieves relative NO_x mitigation compared to fully premixed configurations. To bridge this gap and overcome the intrinsic constraints of conventional industrial burners, this study designed four distinct injection and flow-organization strategies. Traditional swirl burners predominantly utilize fully premixed axial configurations, which are prone to severe nozzle flashback and narrow stability margins when burning low-reactivity NH_3 fuels. In contrast, the present burner architecture decouples the aerodynamic flow routing from the fuel-air mixing state. Tangential oxidizer injection introduces strong circumferential shear to improve flame anchoring, while central non-premixed injection avoids flashback risks under the investigated operating conditions and creates localized fuel-rich zones.

To address these challenges, this study systematically explores the co-firing characteristics of NH_3/CH_4/air swirl flames under four standardized combustion organization modes. Distinct from conventional studies focused primarily on fully premixed or basic air-staged configurations, the main novelties and contributions of this study are threefold: (1) A systematic, decoupled comparison of four combustion organization modes (axial/tangential feeding paired with premixed/non-premixed strategies) is conducted under a high geometric swirl number ($S = 0.769$) across the full NH_3 blending range (η_{NH3} = 0~100%), mapping the flame topology, stability limits, and thermal performance; (2) A weighted comprehensive emission index (iCO + jNO) is proposed, identifying a favorable syner-

gistic C-N trade-off window near $\eta_{NH3} \approx 17\%$ in the tangential non-premixed mode; and (3) CRN modeling and Rate of Production (ROP) analysis reveal that localized fuel-rich reduction micro-zones created by tangential non-premixed injection enhance the reduction consumption of amine radicals toward NO along the key $NH_2 \rightarrow HNO \rightarrow NO$ pathway. These findings provide crucial theoretical insights and technical data for designing stable, low-emission NH_3/CH_4 industrial burners.

2. Experimental and Methods

2.1. Swirl Burner

In this experiment, a self-designed combined swirl-bluff-body burner was employed to generate premixed and non-premixed NH_3/CH_4/air flames. The burner body is fabricated from stainless steel, and its detailed structure is illustrated in Figure 1. The fuel gas is introduced through a central tube and formed into a swirling flow field by swirl vanes in the upper section of the burner. The oxidizer (air, 298 K) enters the burner chamber through a lateral axial inlet and mixes and reacts with the fuel at the total outlet. The system is equipped with a remote-controlled electronic ignition device to ensure safe and rapid ignition.

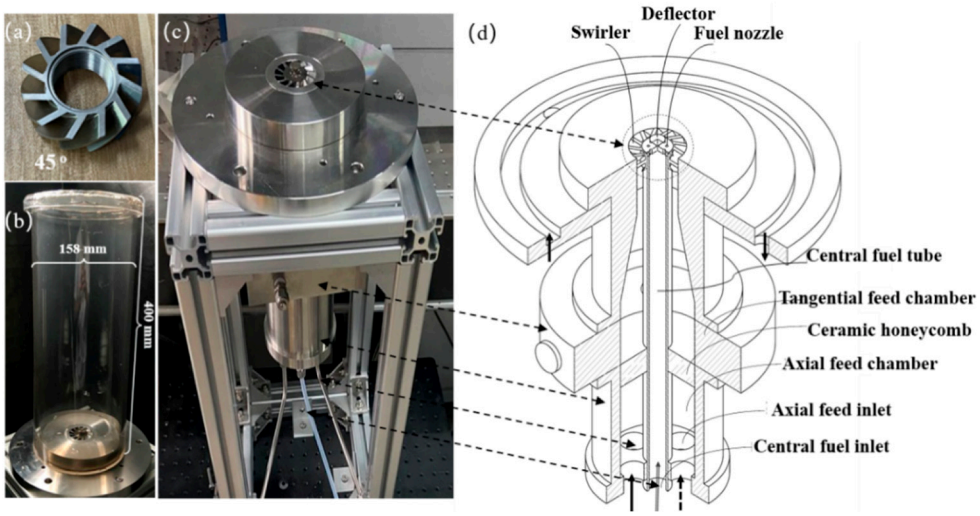


Figure 1. Swirl burner: (**a**) swirler and combustion chamber; (**b**) physical photograph; (**c**) cross-sectional view; (**d**) schematic view.

Both the axial swirler and the concentric inverted-cone stabilizing bluff body are positioned at the total outlet plane at the top of the burner. The swirler consists of 12 straight vanes with a thickness of 2.12 mm, where the vane tip angle θ relative to the central axis is 45°, and the swirler hub diameter (d_i) is 22 mm. Calculated according to Equation (1), the geometric swirl number (S) of this swirler is 0.769, satisfying the technical indicator for generating high-intensity swirl flow ($S > 0.6$) [40]:

$$S = \frac{2}{3} \cdot \frac{1 - (d_i/d_o)^3}{1 - (d_i/d_o)^2} \tan\theta \quad (1)$$

where d_i and d_o represent the hub diameter and outer diameter of the swirler, respectively; θ denotes the angle between the swirl vane and the central axis. The detailed structure is shown in Figure 1a.

The semi-enclosed cylindrical quartz glass combustion chamber used in the experiment is shown in Figure 1b. It features a wall thickness of 10 mm, a diameter of 158 mm, and a height of 400 mm. The design of this chamber not only ensures uniform mixing of

combustion products downstream but also provides an excellent optical pathway for real-time observation of flame topologies and non-intrusive laser diagnostics.

2.2. Experimental System and Methods

The overall configuration of the experimental system is shown in Figure 2 and primarily consists of a gas supply system, a combustion system, a measurement system, connecting pipelines, and a remote automatic ignition device.

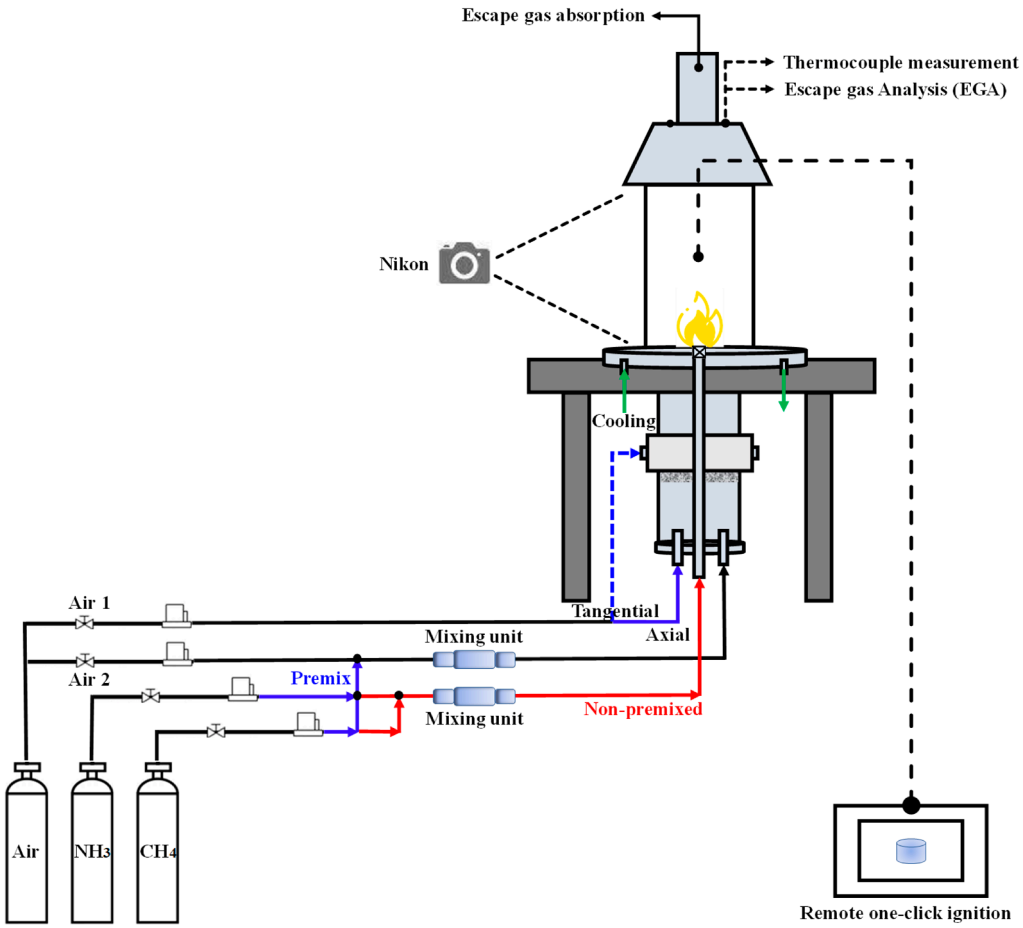


Figure 2. Schematic diagram of the overall configuration of the NH_3/CH_4/air burner and system.

Combustion air is supplied by a compressor and split into two streams after condensation and drying in a refrigerated dryer: one is the primary air (Air1), which controls the axial or tangential injection mode, and the other is the staged air (Air2), which regulates the flow-field balance and premixing. Together, both air streams provide sufficient oxygen for the blended fuel. CH_4 and NH_3 are supplied from high-purity compressed gas cylinders and liquid NH_3 cylinders, respectively (both at 99.99% purity). The flow rate of each gas component is precisely regulated using mass flow controllers (Sevenstar D07-9 model, Beijing Sevenstar Huachuang, Beijing, China) with a measurement accuracy of ±1.0% of the full scale. Given the highly corrosive and alkaline nature of NH_3, the entire transmission pipeline is constructed from polytetrafluoroethylene (PTFE). A dedicated mixing section is installed before the gas mixture enters the burner, containing three sets of static mixers with alternating rotation directions to ensure highly uniform premixing of the multi-route inlets before reaching the burner exit.

This experiment designed four distinct combustion organization modes to modulate the primary air (Air1) entry routes and fuel-air mixing pathways, as illustrated in Figure 3:

(a) axial non-premixed mode, (b) axial premixed mode, (c) tangential non-premixed mode, and (d) tangential premixed mode. To avoid ambiguity, the terms axial and tangential strictly define the aerodynamic inlet routing of the primary swirl air (Air1), whereas the fuel is exclusively introduced centrally or premixed, and is never injected tangentially. Among them, the staged air (Air2) used for flow field balancing is always introduced through the axial inlet. In contrast, the terms "axial" and "tangential" refer specifically to the inlet configuration of the primary swirl air, which is supplied via the bottom axial inlet in the axial modes (Figure 3a,b) and via the side tangential inlet in the tangential modes (Figure 3c,d). During axial mode operation, the tangential inlet is sealed with a custom plug. To clarify the distinct flow paths of each configuration, in the non-premixed modes (Figure 3a,c), the NH_3/CH_4 mixture is fed along the central straight tube directly to the burner exit plane. Conversely, in the premixed modes (Figure 3b,d), fuel is introduced through the bottom annular port to mix with Air1 inside the burner cavity prior to passing through the swirl nozzles. It should be noted that fuel is never introduced tangentially in any case.

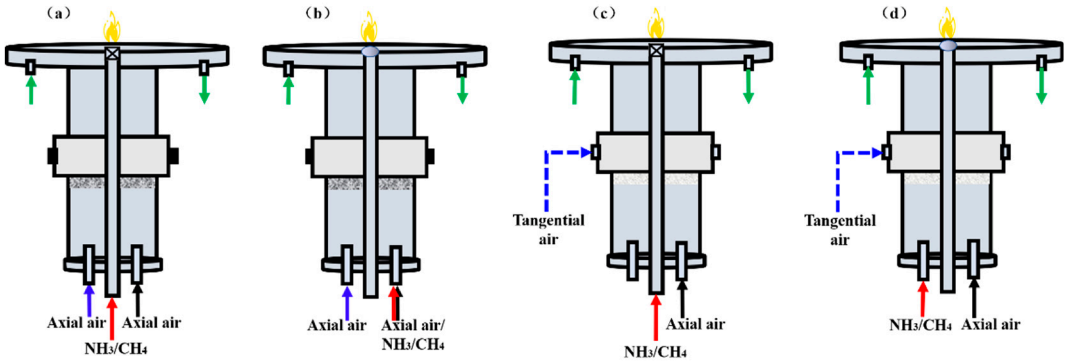


Figure 3. Different combustion modes categorized by primary air routing and mixing state (fuel is injected centrally or premixed, never tangentially): (**a**) axial non-premixed; (**b**) axial premixed; (**c**) tangential non-premixed; (**d**) tangential premixed.

Regarding the fuel injection strategy: in the non-premixed modes, the central fuel tube is connected to the inverted-cone deflecting bluff body and mounted on the base. CH_4 and NH_3 are pre-blended in the mixing section and injected directly through the central fuel inlet to avoid premature contact between the fuel and combustion air. In the premixed modes, a closed deflecting bluff body is used, or the central fuel tube is removed entirely; the axial and tangential feeding chambers are interconnected, and the blended fuel is introduced through sidewall nozzles. Furthermore, an annular cooling water channel is integrated into the outer wall of the top burner base. Circulating cooling water cools the burner in real time, preventing thermal damage to the structure from prolonged overheating.

Online detection of combustion products is performed using an intelligent management platform for industrial boiler environmental monitoring and an online flue gas analyzer (HGA-OES-P01, Foshan Huapuce Intelligent Technology Co., Ltd., Shunde, Foshan, Guangdong, China). The main measured parameters include flue gas oxygen content, moisture content, flue gas outlet temperature, CO, NO, and NO_x concentrations, and system thermal efficiency. An 8 mm outer diameter, high-temperature resistant stainless steel flue gas sampling probe is positioned 100 mm above the downstream exit of the combustion chamber, with a sampling rate of 2 L/min. To prevent water vapor in the flue gas from condensing inside the pipeline and interfering with measurement results, the entire sampling line is wrapped with heating tape and heat-traced throughout the process, preheated to 100 °C before testing. Under each operating condition, flue gas sampling is maintained for 3 min to ensure stable analyzer readings. To ensure data comparability and eliminate

physical dilution effects caused by ambient air entrainment into the downstream sampling collection hood, the raw measured dry pollutant concentrations ($C_{measured}$, dry basis) were normalized to a standard theoretical oxygen reference based on standard combustion evaluation protocols:

$$C_{corrected} = C_{measured} \times \frac{20.9 - O_{2,\ ref}}{20.9 - O_{2,\ measured}} \quad (2)$$

where $O_{2,measured}$ is the simultaneously recorded dry O_2 volumetric percentage, and $O_{2,ref}$ is set to 2.30%, representing the theoretical dry-basis flue gas oxygen concentration under the complete combustion of lean mixtures at $\varphi = 0.90$. This mathematical normalization compensates for aerodynamic entrainment variations across different flame lift-off and injection configurations. Both raw and O_2-normalized values are comparatively evaluated in Section 3.

The flue gas outlet temperature is measured using two K-type thermocouples installed diagonally inside the chimney hood directly above the combustor exit plane. Under each steady-state operating condition, the temperature signals are continuously recorded after thermal stabilization, and the arithmetic mean of the time-averaged readings from the two diagonal thermocouples is taken as the final representative flue gas outlet temperature. It should be noted that the flue gas sampling line incorporates a cold-trap moisture separator upstream of the gas sensors to protect the electrochemical modules. Thus, the measured H_2O concentrations represent residual sample moisture post-conditioning rather than total wet-basis stack gas moisture. The detailed specifications and accuracy of the flue gas analyzer are listed in Table 1.

Table 1. Specifications and accuracy of the flue gas analyzer.

Emission	Sensor Type	Range	Resolution	Accuracy
CO	Electrochemical	0–5000 ppm	1 ppm	±5%
NO	Electrochemical	0–5000 ppm	1 ppm	±5%
NO_x	Calculated	0–5000 ppm	1 ppm	±5%
O_2	Electrochemical	0–25%	0.1%	−0.1% to +0.2% reading
$H_2O(g)$	Electrochemical	0–25%	0.1%	−0.1% to +0.2% reading
$T_{flue\ gas}$	K-Thermoelectric couple	0–1200 °C	0.1 °C	±5%

Repeatability tests conducted before formal experimentation showed that the relative error for the major gas components in the mixture was below 5%. Each condition was repeated 3 to 5 times for error analysis, and the average value was taken after eliminating outliers. Specifically, data points deviating by more than two standard deviations from the sample mean were identified as anomalous fluctuations and excluded. Concurrently, a digital SLR camera (Nikon D90, Nikon Corporation, Tokyo, Japan, resolution 1280 × 1024 pixels) was used to capture instantaneous images of the macro-structure of the swirl flames, with shooting parameters set to an aperture of $f/2$ and an exposure time of 1/25 s. Subsequently, MATLAB 2023b software was used for post-processing tasks such as denoising, enhancement, and sharpening of the flame photographs to extract distinct flame topological features.

2.3. Experimental Conditions

The experiments were conducted at ambient temperature and pressure using NH_3/CH_4/air fuel mixtures. Based on the chemical equations for complete combustion of CH_4 (Equation (3)) and NH_3 (Equation (4)), the stoichiometric air-fuel ratio can be determined:

$$CH_4 + 2O_2 + 7.52N_2 \rightarrow CO_2 + 7.52N_2 + 2H_2O \quad (3)$$

$$NH_3 + 0.75O_2 + 2.82N_2 \rightarrow 3.32N_2 + 1.5H_2O \quad (4)$$

According to the combustion characteristics of the gas mixture, the actual equivalence ratio φ during the testing process is defined as shown in Equation (5):

$$\varphi = \frac{V_{air-stich}}{V_{air-act}} = \frac{3 \times 4.76}{4} \frac{V_{NH_3}}{V_{air}} + 2 \times 4.76 \frac{V_{CH_4}}{V_{air}} \quad (5)$$

where $V_{air-stoich}$ and $V_{air-act}$ are the theoretical stoichiometric air flow rate and the actual supplied air flow rate, respectively. V_{NH3}, V_{CH4}, and V_{air} represent the volumetric flow rates of NH_3, CH_4, and actual air, respectively.

The NH_3 blending ratio η_{NH3} in the blended fuel is defined as the energy share of NH_3 in the total fuel, as expressed in Equation (6):

$$\eta_{NH_3} = \frac{V_{NH_3} LHV_{vol,\ NH3}}{V_{NH_3} \cdot LHV_{vol,\ NH3} + V_{CH_4 \cdot LHV_{vol,\ CH4}}} \times 100\% \quad (6)$$

For comparative analysis, this study conducted co-firing experiments under lean conditions with a fixed equivalence ratio of $\varphi = 0.9$ across various NH_3 blending ratios ($\eta_{NH3} = 0$~100% with a step size of 10%), as detailed in Table 2. To ensure aerodynamic similarity and maintain an approximately constant bulk residence time inside the combustor, the total volumetric mixture flow rate was strictly held constant at 117.8 L/min for non-premixed modes and 122.8 L/min for premixed modes. The minor difference in flow rate (~4.2%) between premixed and non-premixed modes arises from hydraulic balancing between the central injector and annular chambers, resulting in an insignificant bulk residence time variation (<0.16 s) that does not alter the fundamental swirl aerodynamic pattern. Under the constant lean equivalence ratio of $\varphi = 0.9$, as η_{NH3} increases from 0 to 100%, the lower stoichiometric air requirement of NH_3 compared to CH_4 (Equation (4)) dictates that the volumetric fuel throughput increase from 675 cm/s (pure CH_4) to 1571.6 cm/s (pure NH_3) in the non-premixed modes (and 703.4~1637.5 cm/s in the premixed modes), yielding an exact fuel flow growth factor of 2.33 (1571.6/675.0). Concurrently, the combustion air flow rate decreases from 107.63 L/min to 94.08 L/min, with the bulk air velocity shifting from 200.0 cm/s (at pure CH_4) to 174.8 cm/s (at pure NH_3). It should be noted that despite this slight decrease in air velocity, the system operates well above the critical Reynolds number for fully turbulent flow, ensuring that the high-intensity swirl field ($S = 0.769$) and the central toroidal recirculation zone are robustly maintained across all conditions. Consequently, the calculated total thermal input power P_{total} varies slightly within the range of 4.8~6.3 kW across the entire co-firing spectrum. Although these flow velocities and thermal inputs shift intrinsically with the fuel stoichiometry, the shifts are identical across all four modes. The observed performance differences (e.g., a 36.5% reduction in peak CO) substantially exceed the minor confounding influences of flow rate and thermal power variations, confirming that injection and mixing configurations are the governing factors.

Table 2. Operating conditions of NH_3/CH_4/air blended combustion under different η_{NH3}.

Case	Combustion Mode	φ	η_{NH3} (%)	Air Velocity (cm/s)	Fuel Velocity (cm/s)	Total Flow Rate (L/min)
1	Axial non-premixed	0.9	0 → 100	200 → 174.8	675.0–1571.6	117.8
2	Axial premixed				703.4–1637.5	122.8
3	Tangential non-premixed				675.0–1571.6	117.8
4	Tangential premixed				703.4–1637.5	122.8

2.4. Numerical Simulation and CRN Model

To profoundly reveal the kinetic behavior of lean NH_3/CH_4/air combustion and further elucidate the experimental trends observed in the tangential swirl burner, a CRN model was constructed for numerical calculations using ANSYS Chemkin-PRO version 17.2.44. Specifically, this model was tailored to approximate the flow field and multi-stage mixing characteristics of the tangential non-premixed configuration (Case 3), which exhibited the optimal comprehensive performance among the evaluated modes. As shown in Figure 4, the developed CRN architecture simplifies the complex turbulent flow field into a structured network of perfectly stirred reactors (PSRs) and plug-flow reactors (PFRs). This configuration approximates the fuel/oxidizer mixing process, flue gas flow, and recirculation features within the tangential swirl flow, thereby focusing the analysis on the underlying chemical kinetic mechanisms.

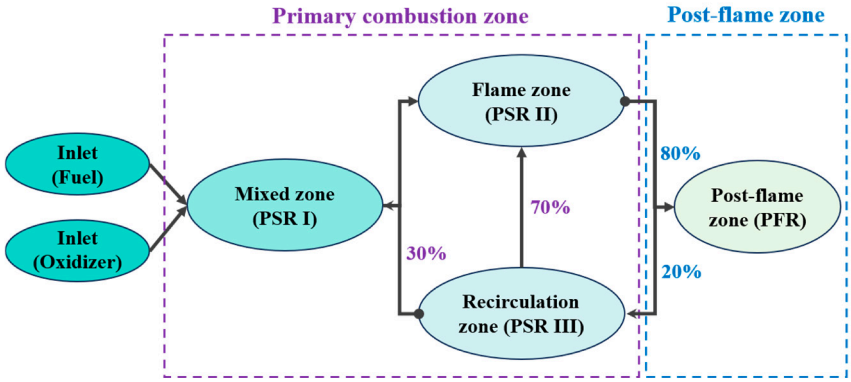


Figure 4. Layout diagram of the CRN model composed of multiple PSRs and PFRs (configured for the tangential swirl non-premixed combustion mode).

Specifically, given that the strong recirculation zone within the swirl burner exhibits uniform temperature and species distributions, the mixing zone near the inlet, the central recirculation zone (CRZ), and the main flame zone are equivalently modeled by three interconnected PSRs to ensure sufficient residence time and high turbulent mixing intensity [41]. Conversely, the downstream main combustion zone and the flue region after swirl dissipation are modeled using a single PFR [42]. The thermodynamic and kinetic parameters of each reactor under steady-state conditions are configured as follows: to isolate the chemical reaction network under the global lean condition ($\varphi = 0.90$), PSR I simulates the unreacted global inlet mixing zone with an initial reaction temperature of 294 K, where total fuel and oxidizer streams are jointly introduced; PSR II represents the main flame zone with its flue gas recirculation fraction fixed at 20%; PSR III represents the CRZ with a recirculation fraction set to 30%, with both high-temperature reactors operating at the lean baseline of $\varphi = 0.90$. The selected recirculation fractions (20% and 30%) are directly supported by established aerodynamic CRN modeling literature for high-intensity swirl burners ($S = 0.769 > 0.6$), where entrainment into the central toroidal recirculation zone typically ranges between 20% and 35% of the primary mass flux [43,44]. Furthermore, the reaction temperatures for PSR II and PSR III are set at an isothermal baseline of 1700 K, corresponding to typical core flame temperatures reported for lean ($\varphi = 0.90$) NH_3/CH_4 swirl combustion [45], while the 3 ms residence time represents the calculated hydrodynamic passage time through the core swirl reaction volume at 117.8 L/min. This isothermal setup effectively decouples fundamental kinetic radical pathways from thermal dissipation confounding factors [45]. Extensive kinetic sensitivity studies in the literature [45] confirm that while operating variations in temperature (100 K) or residence time alter absolute species concentrations, the qualitative emission trajectories and dominant nitrogen

migration paths remain overwhelmingly robust across these parameter bounds. Sensitivity evaluations conducted within ±100 K and recirculation ratios of 15~40% confirm that the relative branching ratios of the primary $NH_2 \rightarrow HNO \rightarrow NO$ pathway vary by less than 8%, demonstrating that the identified kinetic mechanisms are insensitive to moderate variations in the prescribed reactor parameters.

In the numerical simulations, the detailed Okafor kinetic mechanism [46] (comprising 59 species and 356 elementary reactions) was adopted for the CRN calculations. This mechanism has been verified in the literature [47] for high-accuracy prediction of NH_3/CH_4/air flame structures and the evolution of key radicals. Although several comprehensive mechanisms have been proposed recently for NH_3 combustion kinetics (e.g., Stagni et al. [48]), the Okafor mechanism was selected due to its dedicated optimization for NH_3/CH_4/air flames and its validated reliability in predicting flame speed and key nitrogenous pollutant formation. Furthermore, its moderate kinetic scale effectively mitigates numerical stiffness and convergence issues inherent to multi-reactor CRN systems while preserving high fidelity in capturing key NH_2, NH and HNO pathways. Before application, the qualitative trend performance of the model was verified against the measured emission profiles. The inlet boundary conditions of the CRN model are identical to the experimental setups, with the inlet temperature T and pressure P set to 294 K and 0.1 MPa, respectively. The model's validation and calculation scope covers the specific lean condition ($\varphi = 0.90$) and a broad range of NH_3 blending ratios ($\eta_{NH3} = 0$~0.80).

3. Results and Discussion

3.1. Flame Morphology and Operational Stability Limits

Flame morphology is a vital macroscopic feature that characterizes the gas temperature field distribution within the combustor, pollutant emission profiles, and the development of thermal heat fluxes toward the chamber walls and injection ports [49]. Therefore, an in-depth investigation into the evolution of flame morphology under different combustion organization modes is essential to clarify the stability mechanisms of NH_3-blended flames and to optimize exhaust emission control strategies. Under lean conditions ($\varphi = 0.9$), the macroscopic flame morphology evolution images for the four combustion modes across various NH_3 blending ratios ($\eta_{NH3} = 0$~100%) are displayed in Figure 5.

For pure CH_4 combustion ($\eta_{NH3} = 0$), due to the rapid reaction rate and thorough combustion under lean conditions, the overall flame height is low, no obvious soot is formed, and a compact, intensely heat-releasing blue swirling flame is observed. This blue chemiluminescence region is primarily associated with the emission properties of CH* and CO_2 in the reaction zone [50]. Upon introducing a low fraction of NH_3 ($\eta_{NH3} < 30\%$), the reaction zone expands, and its visual appearance gradually shifts to a diffuse yellowish flame. This luminescence transition is primarily linked to $NH_{2\text{-}\alpha}$ radical emissions and thermal radiation from water vapor [51].

As η_{NH3} increases into the moderate-to-high range (30~80%), the combined effect of reduced chemical reactivity and elevated fuel jet velocity (resulting from the fixed total flow strategy to maintain $\varphi = 0.9$) causes the flame front to propagate downstream into the combustor, resulting in continuous flame stretching and an orange-yellow color deepening. Near ≈ 70~80%, the reaction zone detaches from the bluff-body exit plane and migrates downstream, transitioning into a lifted flame accompanied by low-frequency macroscopic oscillations.

When η_{NH3} reaches the critical threshold of 80%, the stability of the premixed and non-premixed flames using the axial feeding strategy deteriorates drastically. Specifically, the axial premixed flame exhibits upstream nozzle flashback, whereas the axial non-premixed flame suffers from severe flame-root detachment and macroscopic aerodynamic-acoustic

pulsations without nozzle flashback (as no oxidizer is present upstream inside the central fuel injector), until the flame undergoes a complete lean blowout at $\eta_{NH3} \approx 85\%$. In contrast, premixed and non-premixed flames that use a tangential feeding strategy exhibit broader operating limits, sustaining combustion even under severe flickering and swaying at $\eta_{NH3} = 90\%$ in the non-premixed mode and successfully reaching continuous combustion up to $\eta_{NH3} = 100\%$ in the premixed mode (Figure 5d). This enhanced stability is attributed to the substantial circumferential momentum imparted by the tangential air inlet, which elevates the effective swirl intensity and strengthens boundary confinement under high NH_3 shares. Comparing the mixing strategies, premixed modes offer wider flammability limits but suffer from elevated flashback risks, whereas non-premixed modes completely avoid nozzle flashback at the expense of a higher lift-off height. Therefore, a comprehensive performance trade-off between these injection and mixing strategies necessitates further quantitative evaluation, incorporating the pollutant emission characteristics and system thermal efficiencies discussed in the following sections.

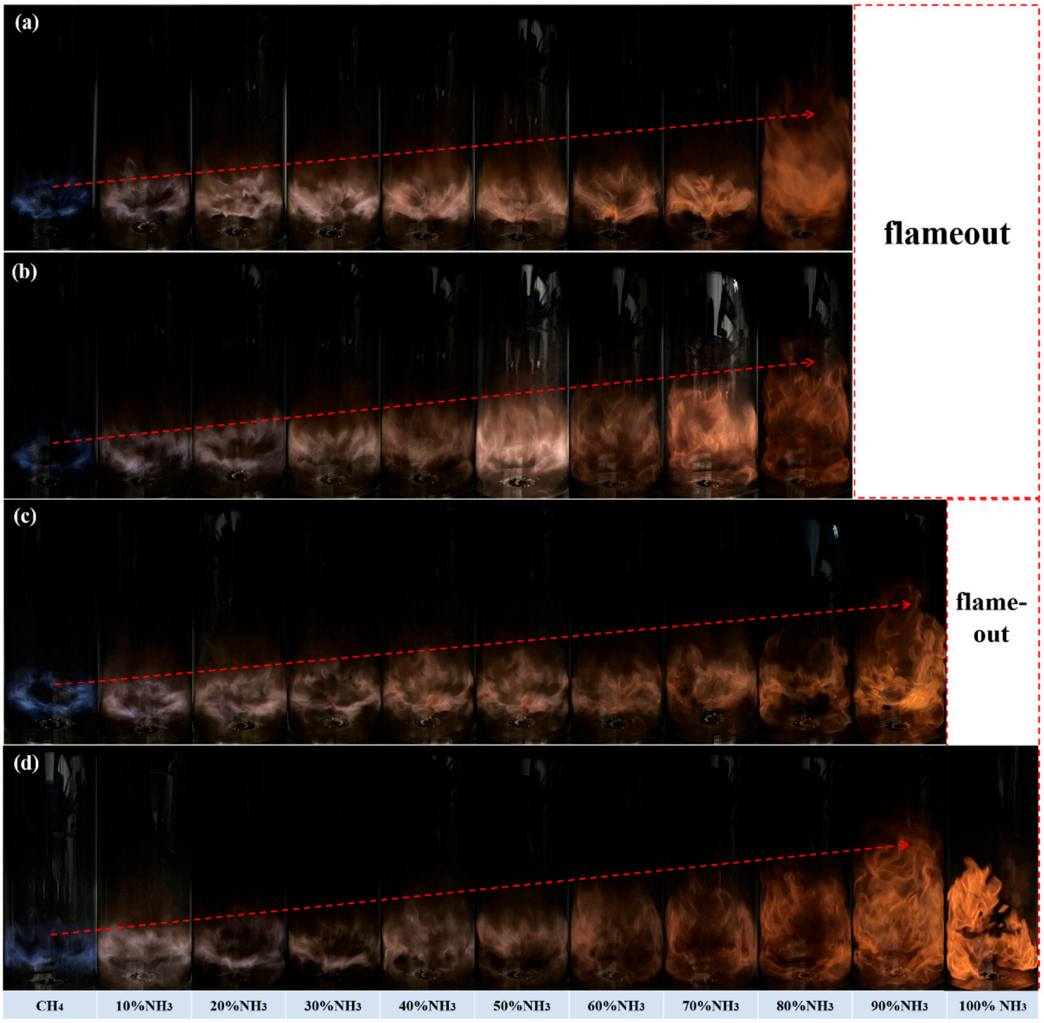


Figure 5. Images of flame morphology variations under different η_{NH3}: (**a**) axial non-premixed; (**b**) axial premixed; (**c**) tangential non-premixed; (**d**) tangential premixed.

3.2. Flue Gas Emission Characteristics

3.2.1. Variations in Flue Gas Oxygen Content, Moisture Content, and Outlet Temperature

Utilizing the intelligent management platform for industrial boiler environmental monitoring and the online flue gas analyzer, the emission characteristics of the swirl flames under

the four combustion organization modes (axial/tangential and premixed/non-premixed) of NH_3/CH_4/air were systematically analyzed. Figure 6 displays the evolution patterns of oxygen content, moisture content, and flue gas outlet temperature in the flue gas under different NH_3 blending ratios (η_{NH3} = 0~100% with a step size of 10%).

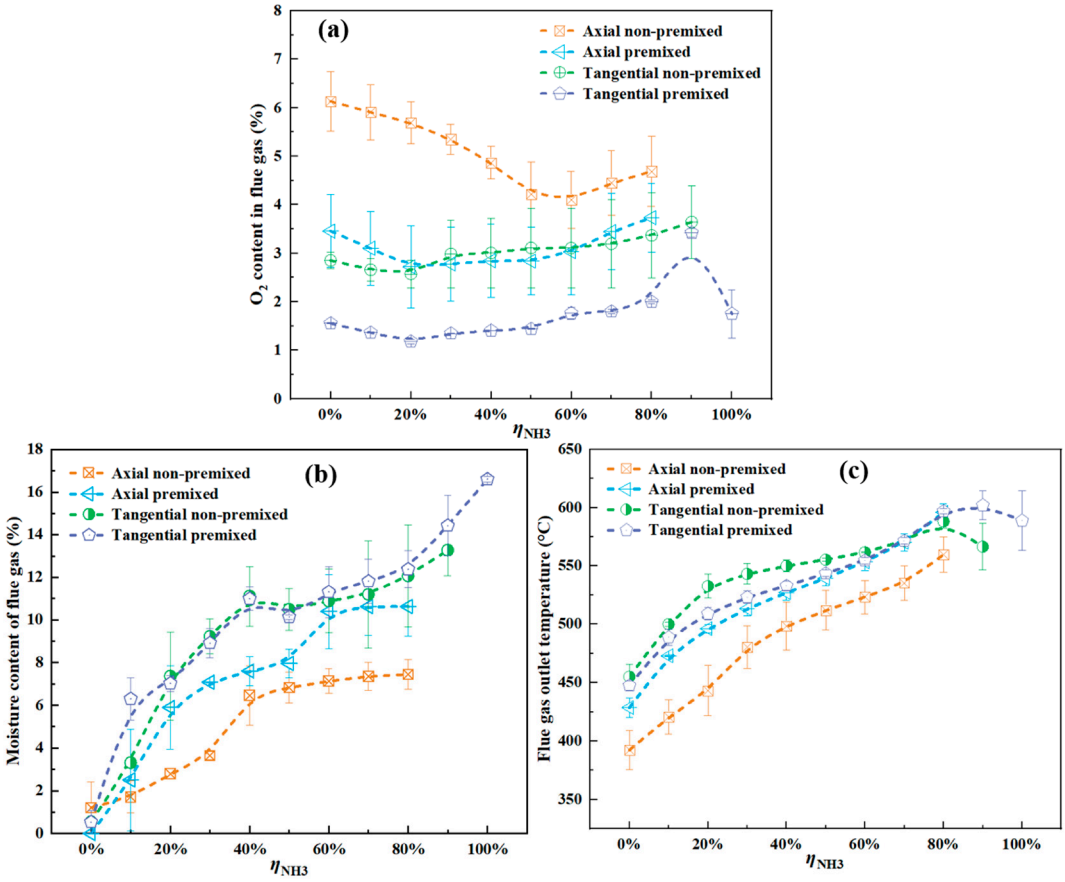


Figure 6. Variations in (**a**) flue gas oxygen content; (**b**) moisture content; and (**c**) flue gas outlet temperature in the four combustion modes under different η_{NH3}.

Analyzing the variation patterns of oxygen content in the flue gas can indirectly reflect the reaction completeness and NH_3/CH_4 co-firing exhaust emission. As illustrated in Figure 6a, which shows the trend of O_2 concentration as η_{NH3} varies from 0 to 100%, it can be observed that as η_{NH3} increases, the O_2 concentration across all modes generally exhibits a non-monotonic trend that first decreases gradually and then rebounds and increases. The actual operating condition is a lean atmosphere ($\varphi = 0.9 < 1.0$) at low η_{NH3}, excess oxygen initially exists in the system, resulting in a higher starting O_2 concentration. As η_{NH3} increases, the oxygen consumption for the oxidation of certain intermediate products (such as CO oxidizing to CO_2) increases, gradually reducing the O_2 concentration in the flue gas to a minimum. At high η_{NH3} conditions, the intrinsic chemical reaction rates slow down, leading to incomplete local energy release, a drop in core flame temperature, and a re-increase in flue gas O_2 concentration. Furthermore, the recorded flue gas O_2 concentrations exhibit localized variations from the theoretical stoichiometric value (~2.3% at $\varphi = 0.9$), which is primarily attributed to ambient air entrainment into the sampling collection hood located 100 mm above the top exit of the semi-enclosed combustor, as well as localized unburned air bypass along the chamber boundary under high flame lift-off conditions. It should be noted that direct online detection of unburnt NH_3 slip was not performed in this study due to measurement equipment limitations; thus, the weakening of combustion

completeness under high NH_3 shares is primarily inferred from the observed thermal drop, reduced chemical reaction fluxes in the CRN model, and elevated flue gas O_2 levels.

Flue gas moisture substantially affects the structural expansion and pollutant formation in NH_3/CH_4 flames. The variations in flue gas moisture content under different combustion modes are shown in Figure 6b. The flue gas moisture content generally increases monotonically with increasing η_{NH3}. In combustion kinetics, water vapor plays a key role in the final NO emission concentration through both chemical and dilution effects. On the one hand, an increase in water vapor can directly enrich the OH radical source in the reaction pool or reduce NO by consuming HNO radicals and NH radicals via the thermal NO_x mechanism. On the other hand, the introduction of moisture also dilutes the NO concentration in the core reaction zone. However, excessive water vapor leads to thermal losses and lowers the local flame temperature, thereby inhibiting the generation rate of OH radicals and weakening the thermal NO formation pathway. Therefore, the effect of water vapor on the final NO emissions depends on the outcome of the competition between promotion and inhibition pathways. Combining Figure 6b with the emission data in Figure 7, it can be found that in the tangential premixed and tangential non-premixed modes, the water vapor concentration undergoes a period of continuous escalation when NH_3 is in the 80~100% range, while the corresponding NO emissions experience a sharp drop during this stage, indicating that the inhibition of flame temperature by moisture and its promotion of NO reduction play a dominant role at this time.

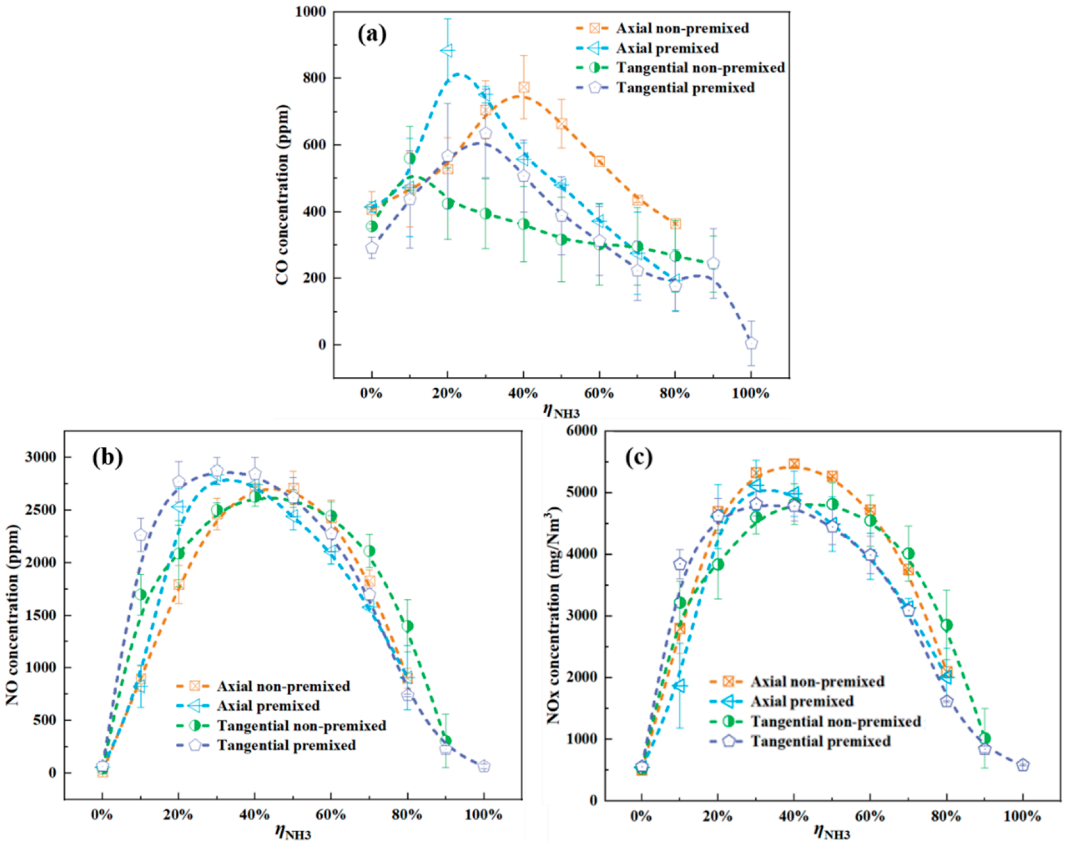


Figure 7. Variations in raw measured dry (**a**) CO, (**b**) NO, and (**c**) NO_x concentration characteristics in the flue gas in the four combustion modes under different η_{NH3} (uncorrected values; corresponding flue gas O_2 levels are shown in Figure 6a. Error bars represent the standard deviations of repeated experimental measurements).

The temperature distribution of combustion products is a critical parameter that determines boiler thermal efficiency and is the core basis for controlling thermal NO_x generation.

To this end, this study quantitatively measured the temperature evolution characteristics of the flue gas outlet of the combustion chamber flame under different η_{NH3}. As shown in Figure 6c, as η_{NH3} increases, the flue gas outlet temperatures across all four combustion modes exhibit an approximately linear increase, indicating that the impact of η_{NH3} on the system's outlet temperature field is well predictable. Within the range of $\eta_{NH3} < 80\%$, the flue gas outlet temperature under the tangential non-premixed mode is overall the highest, the axial non-premixed mode is the lowest, and the temperatures of the axial and tangential premixed modes are intermediate and very close. It is worth noting that in the tangential premixed and tangential non-premixed modes, when NH_3 increases to 80~100%, the flue gas outlet temperature curve exhibits an inflection point followed by a noticeable steep decline. Combined with the aforementioned rising pattern of moisture content, the generation of high-concentration water vapor at high NH_3 fractions significantly reduces the local flame temperature, thereby causing a steep thermodynamic decline in the flue gas temperature at the outlet.

3.2.2. Emission Characteristics of CO, NO, and NO_x Concentrations

CO and NO_x are key characteristic pollutants controlled in the field of NH_3-blended clean combustion. Figure 7 shows the variation in the concentrations of CO, NO, and NO_x (primarily NO, NO_2, and N_2O) in the flue gas across different η_{NH3}. To avoid overstating the experimental evidence, the following evaluations strictly distinguish between the raw measured concentrations, the oxygen corrected emissions, and the theoretically modeled kinetic predictions.

Figure 7a illustrates the variation pattern of CO emissions with NH_3 under lean conditions. As seen from the figure, CO emissions generally show a trend of first increasing and then decreasing with the increase in η_{NH3}. Under high η_{NH3} conditions, CO emissions rapidly decay to near zero, which directly benefits from the intrinsic attribute of NH_3 as a carbon-free fuel. However, when $\eta_{NH3} < 50\%$, CO emissions remain consistently high. According to the Okafor kinetic mechanism [46], CO is an intermediate product of CH_4 oxidation, primarily regulated by the oxidation reactions of CH and HCO radicals with O, O_2, and OH groups, while its consumption is highly dependent on the reaction with OH radicals. Blending NH_3 exhibits a non-linear inhibitory effect on CO emissions. Taking the axial non-premixed and tangential premixed modes as examples, the generation rate of CO is insensitive to changes in the local concentrations of CH/HCO radicals when $\eta_{NH3} < 30\%$, and the introduction of NH_3 fails to effectively cut off the generation pathway of CO, thus unable to lower CO emissions effectively. However, the sensitivity of CO generation to the aforementioned hydrocarbon radicals increases sharply when NH_3 reaches 40%, and NH_3 blending leads to a massive dilution of carbon element concentrations, thereby significantly inhibiting the CO generation reaction and causing a rapid drop in emissions, indicating a transition of the combustion process toward complete combustion. Therefore, appropriately increasing η_{NH3} (>40%) is an effective way to reduce carbon emission intensity substantially.

Based on the experimental results, the overall trends in CO emissions across the four combustion modes are highly consistent, but the emission peaks and the corresponding η_{NH3} ranges differ slightly, all falling within the low η_{NH3} range (15~40%), which indicates that low-ratio NH_3 co-firing can hardly balance carbon reduction benefits. Among them, the tangential non-premixed mode is the first to reach the CO emission peak at $\eta_{NH3} \approx 10\%$, and the peak is only 561 ppm. Whereas the axial and tangential premixed modes reach their peaks within the 20~30% range, with the axial premixed mode exhibiting the highest CO peak (883 ppm) and the tangential premixed mode showing a lower peak (635 ppm). The axial non-premixed mode does not exhibit its emission peak of 775 ppm until $\eta_{NH3} = 40\%$. A comprehensive comparison reveals that the tangential or axial air feeding has a significantly

greater impact on the CO emission peak and its sensitivity range than the premixed or non-premixed mode of organization. Both methods under the tangential feeding mode exhibit lower CO emission peaks, which is attributed to the high swirl intensity brought by the tangential flow field, enhancing the multi-scale species mixing of fuel and air, and increasing the residence time of fluids in the core reaction zone, allowing CO to be more fully oxidized to CO_2. In comparison, the CO emission peak of the tangential non-premixed mode is 36.5% lower than that of the axial premixed mode, making the tangential non-premixed strategy the most beneficial for lowering carbon emission intensity among the four combustion modes.

In the NH_3/CH_4 co-firing system, the emission trend of NO_2 remains highly synchronized with NO, and the absolute emission of NO is more than ten times that of NO_2. Meanwhile, the emission of the potent greenhouse gas N_2O is at least two orders of magnitude lower than that of NO and can be neglected in engineering applications. Although direct experimental measurement of N_2O was not available due to analyzer constraints, our CRN theoretical modeling predicts that N_2O concentrations remain at least two orders of magnitude lower than NO. Acknowledging this diagnostic limitation, definitive conclusions regarding the total NO_x inventory are avoided. Therefore, measured NO concentration is employed as the primary representative indicator for evaluating emission trends, while distinguishing it from calculated NO_x and unmeasured nitrogen intermediates.

As shown in Figure 7b, NO emissions generally increase first and then decrease with increasing NH_3, consistent with the results reported by Zhang [52] and An et al. [53] It is easy to see that there are no NO emissions in the system at $\eta_{NH3} = 0$ (containing only trace amounts of thermal NO). However, once 10% NH_3 is introduced, NO emissions rapidly skyrocket to 500~1000 ppm. At low η_{NH3} (10~30%), the added amount of NH_3 is small, its thermal effect in lowering the flame temperature has not yet manifested, and the high-temperature environment in the combustion zone drives the extensive conversion of N_2 in the air to NO via the thermal mechanism. Concurrently, with the introduction of Fuel-N, the fuel NO generation mechanism rapidly dominates the entire reaction history, and its generation rate far exceeds the potential NO reduction mechanism, thereby causing NO emissions to climb sharply and approach the peak. This indicates that the increase in NO is due to the fuel NO_x mechanism becoming more dominant than the potential NO reduction mechanism as the flame temperature decreases [54]. Under lean conditions, the generation of NO primarily follows the classic NH_3 oxidation kinetic pathway, which is highly dependent on the attack of amine groups by NH_3, OH, and O radicals in the reaction zone. The core reactions include [55,56]: $NH_2 + O \leftrightarrow HNO + H$, $NH + OH \leftrightarrow HNO + H$, and $HNO + OH \leftrightarrow NO + H_2O$. NH_3 blending primarily plays a role in promoting NO generation when $\eta_{NH3} < 50\%$. Whereas when η_{NH3} crosses the critical point of 50%, the presence of high-concentration unburnt NH_3 provides abundant NH_i reducing radicals for the system, thereby triggering the highly efficient gas-phase $DeNO_x$ self-reduction pathways: $4NH_3 + 6NO \rightarrow 5N_2 + 6H_2O$, causing NO emissions to begin dropping significantly, down to a lower level during pure NH_3 combustion. It must be explicitly clarified that while the macroscopic emission trends are direct experimental observations, the specific radical pathways and localized fuel rich zones discussed herein are theoretical mechanisms inferred from the CRN calculations and existing kinetic literature. The present experimental configuration does not directly measure local radical concentrations or spatial distributions.

The maximum NO emissions across all four combustion modes reach comparable plateau magnitudes (2650~2850 ppm raw, and 2675~2930 ppm after O_2 correction). Given the ±5% measurement uncertainty of electrochemical analyzers, the nominal 7.0% variance between the premixed peak (2850 ± 143 ppm) and non-premixed peak (2650 ± 133 ppm) lies within the instrument error band and is not interpreted as an absolute emission-

reduction advantage. Rather, the distinct scientific distinction between these injection strategies lies in the kinetic shifting of the high-risk NO emission window. In premixed modes, homogeneous pre-blending drives prompt fuel-N oxidation, causing the NO concentration to peak rapidly at $\eta_{NH3} \approx 30\%$. Conversely, in non-premixed modes, the requisite spatial diffusion and localized fuel stratification delay the maximum NO generation to $\eta_{NH3} \approx 45\%$. This $\Delta\eta_{NH3} \approx 45\%$ delay provides a broader safe operating envelope in the low-NH_3 transition zone. Therefore, the overall superiority of the tangential non-premixed mode is established not by isolated NO peak suppression, but by its drastic 36.5% reduction in peak CO emissions, wider blow-off limits ($\eta_{NH3} = 90\%$), and an 18.95% lower weighted comprehensive emission index (iCO + jNO).

3.2.3. System Thermal Efficiency, Comprehensive Evaluation of CO and NO

To quantitatively evaluate the impact of different injection strategies on the energy conversion efficiency of the boiler system, a relative thermal efficiency η was calculated using the inverse heat-balance framework based on Chinese National Standard GB/T 10180—2017 [57]:

$$\eta = 100 - \left(\Delta q_1 + \Delta q_2 + \Delta q_3\right) \quad (7)$$

It should be emphasized that η in this study physically serves as a relative combustion-and-thermal conversion efficiency index to assess energy utilization trends across different injection modes under standardized laboratory conditions, rather than an absolute efficiency rating for industrial-scale boilers. While baseline empirical radiation (Δq_3) and fuel calculation coefficients for Δq_1 are adopted from standard tables under identical experimental geometries (Δq_2 is the gas incomplete combustion heat loss rate, %), sensitivity analysis indicates that the exhaust flue gas thermal loss (Δq_1, governed by flue gas outlet temperature) dominates the efficiency variation by over 85%. Although these empirical correlations represent an approximation compared to a direct energy balance for a laboratory setup, their application is justified for relative trend analysis because the directly measured exhaust heat loss overwhelmingly dictates the system's thermal behavior. Considering the measurement accuracies of the flue gas temperature (±5%), flow meters (±1.0%), and CO concentrations (±5%), error propagation yields a relative uncertainty of ±2.1% for the calculated thermal efficiency, which confirms the statistical validity of the comparative trends shown in Figure 8a.

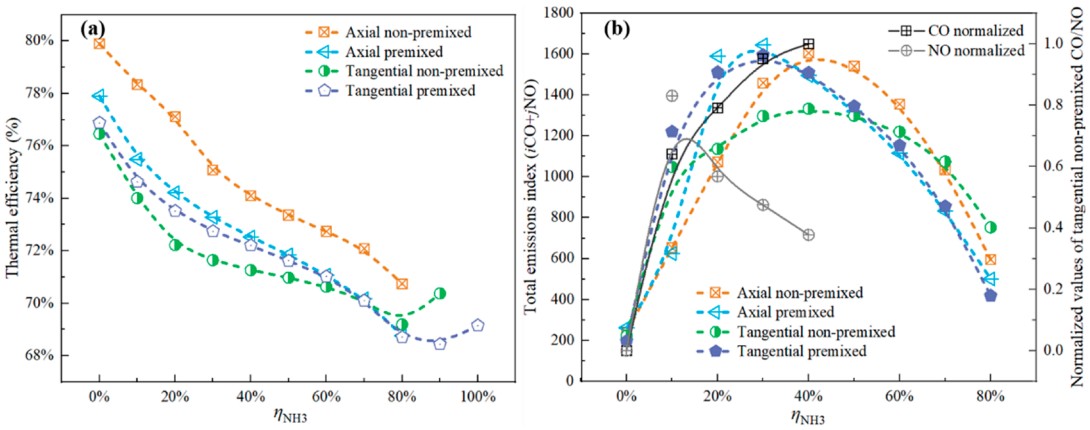


Figure 8. Under different η_{NH3} in the four combustion modes: (**a**) flue gas thermal efficiency; (**b**) the comprehensive iCO + jNO value and the normalized CO/NO values under the tangential non-premixed mode.

Assuming the gas inlet flow rate is x, each heat loss value q is calculated as follows. Among them, the exhaust flue gas heat loss q_1 is quantitatively calculated according to the following Equation (8):

$$\Delta q_1 = [m + n\alpha_{ds}(x)]\left(\frac{t_{ds}(x) - t_{ca}}{100}\right) \quad (8)$$

where m and n are calculation coefficients, taken as 0.50 and 3.45 for natural gas, respectively; α_{ds} is the excess air coefficient at the exhaust, taken as 1.44; t_{ds} is the exhaust temperature, °C; and t_{ca} is the inlet cold air temperature, °C. Although these empirical coefficients are derived for natural gas, sensitivity calculations indicate that applying them across the entire ammonia blending range introduces a maximum relative uncertainty of roughly 3 to 4 percent. Since the exhaust heat loss is predominantly governed by the measured flue gas temperature, this approximation remains scientifically valid for capturing the relative efficiency degradation trend under high η_{NH3} conditions.

The gas incomplete combustion heat loss rate q_2 and heat radiation loss q_3 are obtained by looking up standard specification Tables 3 and 4 [57] using the experimentally measured CO volume fraction and the burner's rated power.

Table 3. Correspondence between gas incomplete combustion heat loss rate q_2 and CO volume fraction [57].

Carbon Monoxide Volume Fraction (ω_{CO})	Gas Incomplete Combustion Heat Loss (q_2%)
$\omega_{CO} \leq 500 \times 10^{-6}$	0.2
$500 \times 10^{-6} < \varphi_{CO} \leq 1000 \times 10^{-6}$	0.5
$\omega_{CO} > 1000 \times 10^{-6}$	1.0

Table 4. Correspondence between heat radiation loss q_3 and rated power [57].

Rated power (MW)	≤2.8	≤4.2	≤7.0	≤10.5	≤14	≤29	≤40
Heat radiation loss q_3 (%)	2.9	2.4	1.7	1.5	1.3	1.1	0.8

Combining the above Equations (7) and (8), the formula for calculating the thermal efficiency of the gas boiler can be expressed as the following Equation (9):

$$\eta = \left(100 - [m + n\alpha_{ds}(x)]\left(\frac{t_{ds}(x) - t_{ca}}{100}\right) - \Delta q_2 - \Delta q_3\right)\% \quad (9)$$

Figure 8a shows the variation in system thermal efficiency with different η_{NH3} for the four combustion modes. The system thermal efficiency under each mode shows a slight decline as η_{NH3} increases, due to the degradation of the fuel's intrinsic heating value and combustion reaction characteristics. This result is similar to Nagatani et al. [58] for boiler NH_3 blending, Nozari et al. [59] for NH_3/H_2 blending in porous combustion media, and Yapicioglu et al. [60] for generator gasoline NH_3 blending. In addition to the lower heating value (LHV) of NH_3, chemical incomplete combustion losses also contribute to this efficiency drop. As η_{NH3} increases, the lower flame temperature and reduced burning velocity inhibit complete intermediate oxidation, resulting in elevated unburned NH_3 slip and residual CO emissions from suppressed CO + OH → CO_2 + H pathways, this increases Δq_2 alongside Δq_1. The absolute difference in thermal efficiency among the four modes is not significant at the same η_{NH3}, with the axial non-premixed mode being the most efficient, only about 2.5% higher than the tangential non-premixed mode, the least efficient. In contrast, the thermal efficiencies of the axial and tangential premixed modes are intermediate and exhibit a high degree of similarity.

As NO and CO emissions exhibit a prominent negative correlation trade-off relationship within the range of $10\% < \eta_{NH3} < 40\%$, to satisfy strict carbon reduction and nitrogen oxide control standards simultaneously, this study referred to the local standard DB 44/765-2019 "Emission standard of air pollutants for boiler" [61], introduced the current CO and NO emission limit values for gas-fired boilers ($I = 200$ ppm and $J = 150$ ppm, respectively), and constructed a weighted comprehensive emission evaluation index iCO + jNO. To strictly align with statutory regulatory constraints, the weight coefficients are defined by the inverse ratio of their allowable limits (i:j = (1/I):(1/J) = (1/200):(1/150) = 3:4), which appropriately imposes a heavier penalty weight on NO emissions. The calculation results are shown in Figure 8b.

From the comprehensive evaluation curves, it is evident that among the four combustion organization modes, the comprehensive emission index peak for the tangential non-premixed mode is lower than those of the other three modes, and it is reduced by 17.64% (approximately 18%) on average. Here, the percentage reduction is defined as $Reduction = \frac{\overline{P}_{other} - P_{tan\text{-}non}}{\overline{P}_{other}} \times 100\%$, where $P_{tan\text{-}non}$ is the peak value of the weighted index iCO + jNO for the tangential non-premixed mode, and $\overline{P}_{other}$ is the mean of the peak values obtained from the remaining three combustion modes. The scientific rationale for using the inverse ratio of statutory limits is to normalize disparate concentrations into dimensionless regulatory compliance penalties, naturally imposing higher penalties on stringently restricted emissions. Sensitivity evaluations across alternative weight ratios from equal weighting to heavy nitrogen penalty show that the peak reduction in the tangential non premixed mode remains consistently within 15% to 22%, confirming that the superiority of this configuration is robust and independent of specific weighting assumptions. Based on the root mean square error propagation method, the relative uncertainty of the corrected emissions and the comprehensive index is estimated at 7.2% and 6.5%, respectively. Because the observed 36.5% peak CO reduction and the 17.64% index reduction significantly exceed these propagated uncertainty bands, the performance superiority of the tangential non premixed configuration is statistically robust. Practically, this signifies that the engineering advantage of this configuration lies not in mitigating the absolute NO peak (which remains comparable within error bounds), but in achieving substantial carbon reduction and delaying the NO surge to provide a safer transitional operating margin. From the perspective of the range corresponding to the peak, the fuel and air are fully mixed in the pipeline beforehand under the premixed mode, and it can reach the chemical reaction activity of a larger substitution share under the non-premixed mode at a lower η_{NH3}, thus its emission peak point appears ahead of the non-premixed mode. Under the tangential non-premixed mode, the comprehensive index increases rapidly in the low η_{NH3} range, approaching about 80% of the peak at η_{NH3} = 10~20%, exhibiting distinct low-ratio sensitivity characteristics.

From a multi-objective trade-off perspective between carbon mitigation and nitrogen oxide regulation, the emission trajectory under the tangential non-premixed mode (Figure 8b) identifies a favorable trade-off operating window near $\eta_{NH3} \approx 15\%$~20% (centered around ~17%). It should be clarified that this ~17% value represents an estimated operating window derived from the interpolated trends of the weighted index, rather than a strictly validated singular optimum point through additional high-resolution measurements. Within this transitional regime, the intermediate CO concentration has already decreased by >35% from its initial low-ratio peak (561 ppm at η_{NH3} = 10%) due to enhanced swirl-mixing oxidation, whereas the NO concentration remains within moderate bounds before entering the exponential fuel-NO_x surge governed by the HNO + H → H_2 + NO pathway (which accelerates sharply at $\eta_{NH3} \geq 30\%$, as revealed in Section 3.3). This kinetic confluence allows the system to achieve an optimal synergistic C-N emission compromise at $\eta_{NH3} \approx 17\%$ alongside sustained high thermal efficiency (>74%).

Although flue gas NH_3 concentration was not directly measured due to sensor hardware constraints, a high degree of NH_3 conversion near $\eta_{NH3} \approx 17\%$ is strictly a kinetic inference from the thermal plateau and radical pool simulations rather than an experimentally quantified concentration. As NH_3 levels remain low, the abundant OH and H radical pool supplied by CH_4 oxidation drives extremely fast NH_i consumption kinetics, and the high thermal release plateau confirms negligible unburned chemical heat loss, suggesting high fuel utilization rather than a directly quantified slip concentration. Combining the aforementioned research results on the steady range of flame topological structures in Figure 5, it can be concluded that the air-staged strategy of injecting NH_3 gas through the central fuel tube while introducing tangential primary air and axial staged air is the most effective combustion construction scheme. Consequently, among the four specific combustion organization modes compared, the tangential non-premixed mode performs best across a range of thermal combustion characteristics, including flame stability, C-N synergistic emission reduction response, and system thermal efficiency.

It is worth noting that while recent studies (e.g., Mashruk et al. [62], Li et al. [63]) have emphasized that N_2O emissions can sometimes increase as NO_x decreases under ultra-lean or low-temperature quenched conditions, N_2O was neglected in our primary experimental trade-off due to analyzer sensor limitations. The low N_2O concentration (<10 ppm) discussed herein represents a theoretical kinetic prediction from our CRN model under high flame temperatures (1550 K~1750 K), which should be noted as a diagnostic limitation rather than an experimentally verified result. At flame temperatures above 1400 K, N_2O undergoes rapid thermal decomposition via $N_2O + H \rightarrow N_2 + OH$, preventing its accumulation in the high-temperature swirl flow field. Note that the current 0-D CRN model mainly isolates the global homogeneous kinetics. The exact localized turbulence-chemistry interactions induced by the non-premixed shear layers should be further verified using high-fidelity simulations (e.g., Large Eddy Simulation) in future work.

3.3. CRN and Kinetic Mechanism Analysis of NO Formation

To profoundly reveal the core kinetic behavior in the NH_3/CH_4/air co-firing flow field at the molecular elementary reaction level, this study prioritized the tangential non-premixed mode with superior comprehensive performance, and quantitatively extracted the rates of the top 10 elementary reactions for NO generation and consumption within the main flame region using the CRN model. Figure 9 lists the dominant elementary reaction pathways under three typical NH_3 blending cases ($\varphi = 0.90$).

Under the low NH_3 case of $\eta_{NH3} = 10\%$, the NO generation within the system is primarily controlled by the reaction $NO_2 + H \rightleftharpoons NO + OH$, while the generated NO subsequently reacts rapidly with HO_2, O, and H radicals via reverse radical recombination reactions to be consumed. At this stage, because the total amount of fuel nitrogen is small, the thermal NO generation pathway via high-temperature oxidation of N_2 still dominates the network, keeping the absolute generation rate and net accumulation of NO relatively low.

At the moderate NH_3 case of $\eta_{NH3} = 30\%$, the elementary reaction $HNO + H \rightleftharpoons H_2 + NO$ leaps to become the primary NO generation channel in the system. Concurrently, the reaction rates of NH and O accelerate, leading to a localized net increase in the generation rate of NO that far exceeds the 10% NH_3 condition. From the perspective of reaction kinetics, although the increase in η_{NH3} at this time reduces the core zone temperature of the flame and inhibits the traditional thermal NO generation to a certain extent, the massive introduction of NH_3 enriches the system with extremely abundant HNO intermediates. These HNO intermediate products react violently with OH and H radicals in the reaction pool, inducing an extremely high fuel NO generation rate. Although the increase in NH_3 share also elevates the NH radical concentration, which accelerates the rates of reduction

consumption reactions such as NH + NO ⇌ N_2O + H, the absolute flux of oxidation generation is much larger than the reduction flux, so the absolute generation of NO in the flue gas exhibits explosive growth.

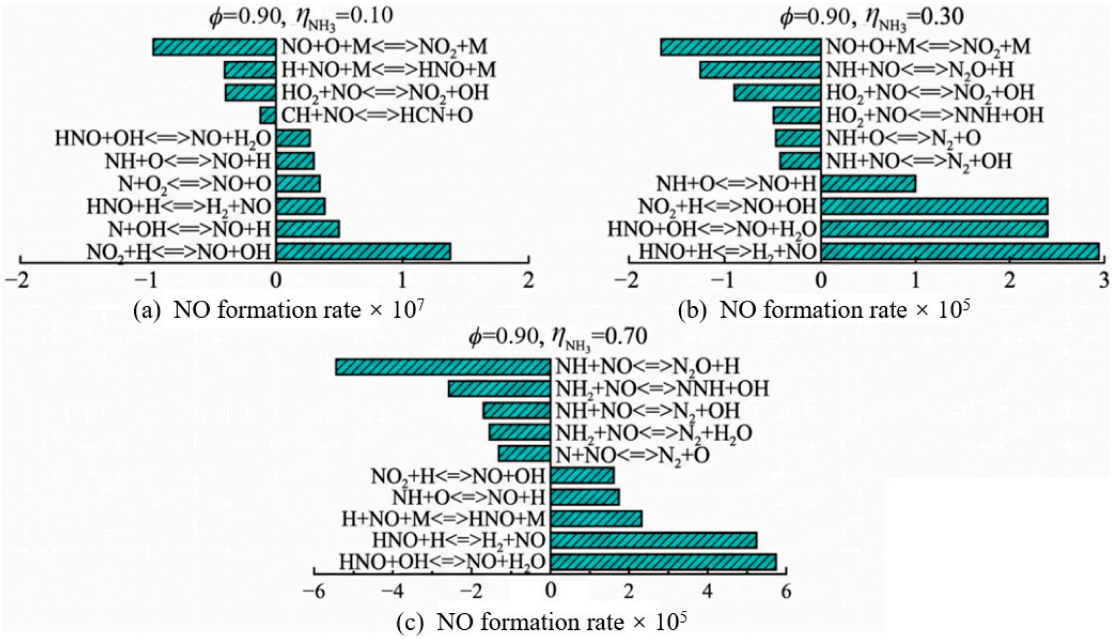


Figure 9. Absolute rates of NO generation in the main flame zone of NH_3/CH_4 blended fuel combustion derived from CRN modeling (Positive values indicate net NO formation and negative values denote net NO consumption).

Under the high NH_3 case of η_{NH3} = 70% (evaluated under the global lean condition of φ = 0.90), the reactions HNO + OH ⇌ NO + H_2O and HNO + H ⇌ H_2 + NO jointly constitute the two primary pathways for NO generation. Concurrently, the intermediate HNO accelerates thermal decomposition via the collision dissociation effect of the third body M, further broadening the chemical source of NO release. However, the contributions of amine radicals (NH and NH_2) and atomic N to the selective catalytic reduction in NO become increasingly prominent at this stage. As evidenced by the negative net reaction rates in Figure 9c, the substantial accumulation of amine intermediates inherently activates dominant gas-phase $DeNO_x$ self-reduction pathways (such as NH + NO ⇌ N_2O + H and NH_2 + NO ⇌ N_2 + H_2O). In the physical burner, this kinetic self-reduction propensity is further facilitated by the non-premixed injection strategy, where spatial fuel stratification provides localized reaction zones that favor NH_i-NO interactions prior to complete oxidizer mixing, thereby greatly increasing the flux of reduction reactions, significantly weakening the overall propensity for NO generation, and effectively curbing emissions under high NH_3 shares. It should be acknowledged as a methodological limitation that the zero-dimensional CRN framework evaluates these kinetic pathways under simplified homogeneous reactor assumptions. Consequently, it isolates chemical reaction fluxes but does not capture localized turbulence–chemistry interactions, steep radical gradients, or finite-rate micromixing within the non-premixed shear layers. In summary, the mutual conversion between NO and NO_2 within the core reaction zone, along with the evolution of the intermediate HNO, constitutes the core kinetic network of NO formation under the NH_3 co-firing system. It should be noted regarding Figure 9 that all elementary reaction rates are expressed in units of mole/(cm^3·s), where positive values represent net NO formation and negative values denote net NO reduction or consumption. In Figure 9a (η_{NH3} = 0.10), the reaction rates are on the order of 10^{-7} mole/(cm^3·s) due to low fuel-N input and background thermal-NO

dominance. In contrast, at $\eta_{NH3} = 0.30$ and 0.70 (Figure 9b,c), the reaction rates surge by two orders of magnitude to 10^{-5} mole/(cm^3·s), driven by the rapid activation of fuel-NO_x kinetic pathways.

To further clarify the element migration behavior inside the reaction network, a quantitative ROP conservation analysis was performed on the NO generation pathways under different η_{NH3}, and the results are shown in Figure 10. The spatial direction of the arrows indicates the chemical evolution of nitrogen, and its corresponding value indicates the percentage contribution rate of each elementary reaction pathway to NO generation or consumption. Specifically, the percentage assigned to each pathway branch in Figure 10 is normalized using the total consumption (or production) rate of the originating precursor species as the denominator (e.g., for reactant X, the branching ratio is defined as $100\% \times \mathrm{ROP}\ (X \rightarrow Y)/\sum \mathrm{ROP}_{\text{total consumption of X}}$).

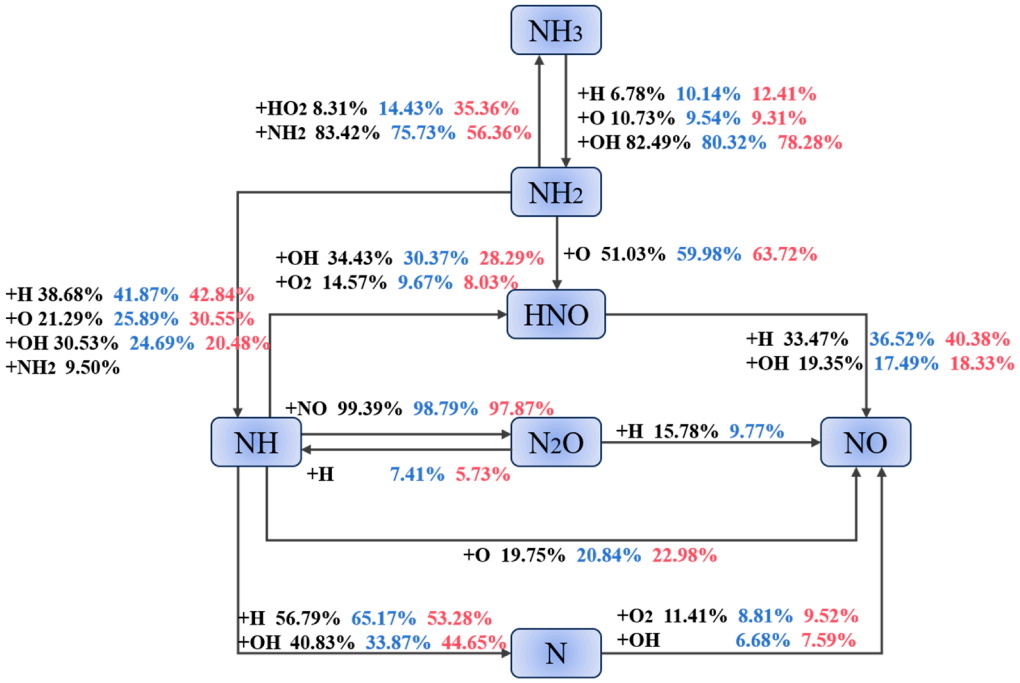


Figure 10. Analysis of NO generation pathways for NH_3/CH_4 blended fuel combustion (black text for 10% NH_3 ratio, blue text for 30% NH_3 ratio, red text for 70% NH_3 ratio).

Analysis shows that the primary generation pathway of NO in the co-firing blended fuel begins with the migration of NH_3 toward NH_2 or NH radicals via consecutive dehydrogenation reactions. Subsequently, the evolved amine groups generate NO primarily through four characteristic kinetic branches: (1) NH → NO; (2) NH → N_2O → NO; (3) NH → N → NO; (4) NH_2 (NH) → HNO → NO. Among these four competing branches, HNO → NO represents the primary pathway for nitrogen conversion, with NH_2 → HNO serving as the principal source of HNO intermediates. Therefore, under different η_{NH3} conditions, the primary NO generation kinetic backbone of the blended fuel can be abstracted into the backbone pathway of NH_2 → HNO → NO, while another important pathway is NH_2 → NH → HNO → NO. In this evolution process, NH_3 undergoes collisions with high-energy H, O, and OH radicals in the flow field and dehydrogenates to generate NH_2, which then continuously reacts with these active groups to convert into more active NH or HNO radicals, finally releasing NO under the attack of OH and H. Fundamental physical and chemical facts indicate that each key dehydrogenation and oxidation step in this kinetic network is highly dependent on the local concentration levels of OH and H radicals in the reaction pool. This pathway analysis conclusion is consistent with the microscopic calcu-

lation results for the NO generation rate in Figure 9, fully confirming that the elementary reactions converting to NO via the HNO intermediate yield the highest net contribution in the entire co-firing system.

4. Conclusions

Using a self-designed combined swirl-bluff-body burner, this study systematically investigated the effects of different injection strategies and NH_3 blending ratios on the topological structure, stability, flue gas emission characteristics, and micro-reaction kinetic mechanisms of NH_3/CH_4/air swirl co-firing flames through experimental measurements and numerical simulations of chemical reactor networks. The primary conclusions are as follows:

- With the increase in the NH_3 blending ratio, due to the degradation of the overall fuel reaction reactivity and heat release intensity, the flames under all four combustion organization modes gradually stretch and evolve from a compact blue V-shaped topological structure during pure CH_4 combustion to an orange-yellow M-shaped envelope structure, transitioning into a violently oscillating lifted detached state during the high NH_3 share stage. In terms of aerodynamic flow field characteristics, the tangential feeding strategy demonstrates superior blowout resistance and a broader flammability operating range than the axial feeding strategy, thereby sustaining continuous combustion even under quasi-limit conditions with an NH_3 blending ratio of 90% in the non-premixed mode and up to pure NH_3 in the premixed mode, while completely avoiding the nozzle flashback risks observed in axial premixed configurations under the investigated operating conditions.
- At the lean equivalence ratio, CO and NO emissions in the flue gas both present a trend of first increasing and then decreasing with the increase in the NH_3 blending ratio, regardless of sample dilution correction. While peak NO emission magnitudes remain comparable across modes (2650~2850 ppm), non-premixed injection delays the high-risk NO peak window ranges of 30~45% NH_3 blending ratios due to spatial diffusion stratification. Beyond 50%, the abundant amine radicals in the reaction zone can reduce NO to nitrogen gas via highly efficient amine-radical-mediated reaction pathways, resulting in a steep reduction in measured NO down to low baseline levels under pure NH_3 co-firing.
- The aerodynamic inlet routing (tangential and axial) exerts a dominant influence on carbon burnout and flame stability compared to the mixing state. Strong circumferential shear vortices induced by tangential feeding enhance fluid residence time and species mixing, reducing the peak CO emission in the tangential non-premixed mode by 36.5% compared to the axial premixed mode. Comprehensive evaluation using the normalized, dilution-compensated index iCO + jNO confirms an approximate 18% average peak reduction for the tangential non-premixed mode, identifying a favorable synergistic C-N trade-off window near the NH_3 blending ratio of 15~20% (~17%) with high thermal efficiency and sustained stability up to a 90% ratio in the non-premixed mode (and 100% in the premixed mode).
- The chemical reactor network model and the quantitative rate of production conservation analysis reveal that the primary nitrogen element migration network of the co-firing blended fuel is dominated by the backbone pathway of $NH_2 \rightarrow HNO \rightarrow NO$ under different NH_3 blending ratios. Under the moderate NH_3 case, the elementary reaction $HNO + H \rightarrow H_2 + NO$ becomes the dominant reaction channel, causing the fuel NO_x generation rate to far exceed the reduction mechanism. Under high NH_3 conditions (≥70%), the CRN calculations confirm that the extensive buildup of NH_i intrinsically activates dominant $DeNO_x$ self-reduction pathways ($NH + NO \rightarrow N_2O + H$,

$NH_2 + NO \rightarrow N_2 + H_2O$), yielding a net negative NO formation rate. In practical burner operation, non-premixed injection physically complements this kinetic mechanism by providing fuel-stratified reaction zones that sustain localized NH_i-N interactions, effectively curbing the net generation of pollutants at the molecular level under high NH_3 shares.

Overall, while this study was conducted on a laboratory scale, the findings may offer useful reference points for industrial NH_3/CH_4 co-firing applications. The tangential non-premixed strategy provides a practical reference for swirl burner concepts to mitigate flashback risks while maintaining flame stability. Additionally, the identified low NH_3-doped window (≈17%) and CRN kinetic insights may serve as helpful baseline data for optimizing co-firing operation and calibrating numerical models in future application developments. It must be explicitly acknowledged that unreacted NH_3 slip and N_2O emissions were not experimentally quantified in this study due to diagnostic constraints. Moreover, the CRN modeling represents a simplified zero dimensional approximation of the combustion system that cannot fully capture localized turbulence chemistry interactions. However, direct extrapolation to industrial burners must explicitly account for scale effects, geometric dependence, elevated operating pressures, and differing heat loss behaviors.

Author Contributions: Conceptualization, P.L. and C.L.; methodology, F.D. and Y.W. (Yong Wang); validation, X.Z. and X.Q.; resources, B.K.; data curation, Y.W. (Youxing Wei); writing—review and editing, Y.W. (Youxing Wei); supervision, P.L., F.D., Y.W. (Yong Wang), X.Z., X.Q. and B.K.; funding acquisition, B.K. All authors have read and agreed to the published version of the manuscript.

Funding: This research was supported by the Natural Science Foundation of Jiangxi Province of China (Grant No. 20262BAC200251) and the Jiangxi Province Program for the Early Career Development of Young Scientific and Technological Talents (Grant No. 20262BEJ730460).

Data Availability Statement: The data presented in this study are available from the corresponding author upon reasonable request.

Acknowledgments: The authors would like to thank the School of Electrical Engineering, Jiangxi University of Water Resources and Electric Power, for its support in this research.

Conflicts of Interest: The authors declare no conflicts of interest. The funders had no role in the design of the study; in the collection, analyses, or interpretation of data; in the writing of the manuscript; or in the decision to publish the results.

References

1. Qiao, L.; Wang, H.; Chen, P.; Gu, M.; Luo, K.; Hu, X. The influence mechanism of CO_2 on the transformation of nitrogen-containing components in ammonia-coal co-firing: An experimental and kinetic mechanism investigation. *Combust. Flame* **2026**, *283*, 114585. [CrossRef]
2. Jia, Q.; Zhang, T.; Zhu, Z.; Cai, R.; Song, K.; Yan, F.; Qayyum, A. Harnessing hydrogen energy storage for renewable energy stability in China: A path to carbon neutrality. *Int. J. Hydrogen Energy* **2025**, *118*, 93–101. [CrossRef]
3. Mao, F.; Lin, J.; Hou, Y. Dynamic evolution and frontiers of energy decentralization research: A bibliometric-based review. *Energy Strateg. Rev.* **2026**, *64*, 102097. [CrossRef]
4. Tarhan, C.; Çil, M.A. A study on hydrogen, the clean energy of the future: Hydrogen storage methods. *J. Energy Storage* **2021**, *40*, 102676. [CrossRef]
5. Valera-Medina, A.; Marsh, R.; Runyon, J.; Pugh, D.; Beasley, P.; Hughes, T.; Bowen, P. Ammonia-methane combustion in tangential swirl burners for gas turbine power generation. *Appl. Energy* **2017**, *185*, 1362–1371. [CrossRef]
6. Wang, Q.; Zhang, P.; Liu, C.; Yang, B. Co-oxidation of ammonia with ethylene and acetylene: An experimental and kinetic modeling study. *Combust. Flame* **2026**, *284*, 114630. [CrossRef]
7. Wei, Y.; Sun, J.; Cai, J.; Xia, Y.; Lin, Z.; Xi, Z.; Lu, Z.; Yao, S. Experimental and DFT study on the NH_3/O_2 adsorption characteristics and mechanism in NH_3/coal co-firing. *Int. J. Hydrogen Energy* **2026**, *211*, 153545. [CrossRef]
8. Abubakar, S.; Li, Y. Ammonia-fueled internal combustion engines: A review of research trends. *Fuel* **2026**, *406*, 137016. [CrossRef]

9. Mobasheri, R.; Rezaei, H.; Taher, R.; Ali, S.; Khaled, M. Combustion and emission control of hydrogen–ammonia blends in internal combustion engines. *Energy Convers. Manag. X* **2026**, *31*, 101945. [CrossRef]
10. Si, T.; Wang, K.; Wang, X.; Yang, Y.; Ma, P.; Li, S. Flexible ammonia/coal injection on NOx emissions and combustion characteristics in a 500-kW one-dimensional furnace under low-load condition. *Proc. Combust. Inst.* **2025**, *41*, 105916. [CrossRef]
11. Liu, M.; Chen, S.; Zhu, H.; Xu, J. Numerical study on flame structure and NOx generation under different Coal/NH_3 co-firing strategies in a 1000 MW utility boiler. *J. Energy Inst.* **2025**, *119*, 101957. [CrossRef]
12. Türkkahraman, Z.; Alabaş, B. Effect of oxy-fuel combustion on temperature, flame speed and NO_X emission values of methane-ammonia flames in a model gas turbine combustor. *Fuel* **2026**, *422*, 139138. [CrossRef]
13. Uddeen, K.; Tang, Q.; Shi, H.; Turner, J. Performance and emission analysis of ammonia-ethanol and ammonia-methane dual-fuel combustion in a spark-ignition engine: An optical study. *Fuel* **2024**, *358*, 130296. [CrossRef]
14. Ma, C.; Cui, B.; Du, Y.; Yu, Z.; Du, J.; Wang, Y. NOx formation in pulverized coal co-firing with ammonia and hydrogen: Effects of fuel properties and air-staging. *J. Energy Inst.* **2026**, *124*, 102409. [CrossRef]
15. Zhang, W.; Liu, X.; Zhang, C.; Li, M.; Niu, T.; Xie, Y.; Wang, H. Industrial scale testing on the combustion and NOx emission characteristics of ammonia cofiring in a 40 MWth coal-fired boiler. *Fuel* **2024**, *359*, 130471. [CrossRef]
16. Chen, P.; Wang, H.; Qiao, L.; Gu, M.; Luo, K.; Fan, J. Study of the NO formation characteristics and ammonia-N/coal-N transformation mechanism of ammonia-coal co-combustion in O_2/CO_2 atmosphere. *Combust. Flame* **2024**, *270*, 113756. [CrossRef]
17. Ma, L.; Li, K.; Fang, Q.; Chen, G.; Zhang, C. A novel swirl burner with coal co-firing ammonia: Effect of extension length of the dual-channel ammonia pipe on combustion and NOx formation. *Int. J. Hydrogen Energy* **2024**, *78*, 344–352. [CrossRef]
18. Zhang, B.; Qu, M.; He, W.; Pang, B.; Yu, R.; Zhang, K.; Xie, Z.; Liu, X.; Xu, Y. A novel low-NO burner with in-burner high-speed air jet array for ammonia-coal co-firing: Integrating ammonia pyrolysis and deep air staging. *J. Energy Inst.* **2025**, *119*, 101952. [CrossRef]
19. Wang, S.; Wei, X.; Gu, M.; Lin, Q.; Luo, G.; Hu, F. Flame characteristics and NO emission law of sliding arc plasma-assisted ammonia combustion. *Combust. Flame* **2025**, *274*, 114000. [CrossRef]
20. Yan, W.; Ren, J.; Feng, J.; Duan, Y.; Wei, C. A new forest fire risk rating forecast model based on XGBoost. In Proceedings of the 2022 International Seminar on Computer Science and Engineering Technology (SCSET), Indianapolis, IN, USA, 8–9 January 2022; pp. 227–230.
21. Yang, Y.; Huang, Q.; Sun, J.; Ma, P.; Li, S. Reducing NOx emission of swirl-stabilized ammonia/methane tubular flames through a fuel-oxidizer mixing strategy. *Energy Fuels* **2022**, *36*, 2277–2287. [CrossRef]
22. Han, X.; Wang, Z.; Costa, M.; Sun, Z.; He, Y.; Cen, K. Experimental and kinetic modeling study of laminar burning velocities of NH_3/air, NH_3/H_2/air, NH_3/CO/air and NH_3/CH_4/air premixed flames. *Combust. Flame* **2019**, *206*, 214–226. [CrossRef]
23. Tang, G.; Jin, P.; Bao, Y.; Chai, W.S.; Zhou, L. Experimental investigation of premixed combustion limits of hydrogen and methane additives in ammonia. *Int. J. Hydrogen Energy* **2021**, *46*, 20765–20776. [CrossRef]
24. Ge, Y.; Ma, H.; Wang, L. Kinetic modeling and experimental study of laminar burning velocities of $CH_4/NH_3/N_2O$/Ar premixed flames. *Combust. Flame* **2025**, *278*, 114253. [CrossRef]
25. Xiao, H.; Howard, M.; Valera-Medina, A.; Dooley, S.; Bowen, P.J. Study on reduced chemical mechanisms of ammonia/methane combustion under gas turbine conditions. *Energy Fuels* **2016**, *30*, 8701–8710. [CrossRef]
26. Kurata, O.; Iki, N.; Matsunuma, T.; Inoue, T.; Tsujimura, T.; Furutani, H.; Kobayashi, H.; Hayakawa, A. Performances and emission characteristics of NH3–air and NH_3CH_4–air combustion gas-turbine power generations. *Proc. Combust. Inst.* **2017**, *36*, 3351–3359. [CrossRef]
27. Okafor, E.C.; Somarathne, K.D.K.A.; Ratthanan, R.; Hayakawa, A.; Kudo, T.; Kurata, O.; Iki, N.; Tsujimura, T.; Furutani, H.; Kobayashi, H. Control of NOx and other emissions in micro gas turbine combustors fueled with mixtures of methane and ammonia. *Combust. Flame* **2020**, *211*, 406–416. [CrossRef]
28. Zhu, X.; Khateeb, A.A.; Guiberti, T.F.; Roberts, W.L. NO and OH* emission characteristics of very-lean to stoichiometric ammonia–hydrogen–air swirl flames. *Proc. Combust. Inst.* **2021**, *38*, 5155–5162. [CrossRef]
29. Zhu, X.; Khateeb, A.A.; Roberts, W.L.; Guiberti, T.F. Chemiluminescence signature of premixed ammonia-methane-air flames. *Combust. Flame* **2021**, *231*, 111508. [CrossRef]
30. Mashruk, S.; Xiao, H.; Valera-Medina, A. Rich-Quench-Lean model comparison for the clean use of humidified ammonia/hydrogen combustion systems. *Int. J. Hydrogen Energy* **2021**, *46*, 4472–4484. [CrossRef]
31. Khateeb, A.A.; Guiberti, T.F.; Zhu, X.; Younes, M.; Jamal, A.; Roberts, W.L. Stability limits and exhaust NO performances of ammonia-methane-air swirl flames. *Exp. Therm. Fluid Sci.* **2020**, *114*, 110058. [CrossRef]
32. Khateeb, A.A.; Guiberti, T.F.; Wang, G.; Boyette, W.R.; Younes, M.; Jamal, A.; Roberts, W.L. Stability limits and NO emissions of premixed swirl ammonia-air flames enriched with hydrogen or methane at elevated pressures. *Int. J. Hydrogen Energy* **2021**, *46*, 11969–11981. [CrossRef]
33. Li, S.; Zhang, S.; Zhou, H.; Ren, Z. Analysis of air-staged combustion of NH_3/CH_4 mixture with low NOx emission at gas turbine conditions in model combustors. *Fuel* **2019**, *237*, 50–59. [CrossRef]

34. Wei, X.; Zhang, M.; An, Z.; Wang, J.; Huang, Z.; Tan, H. Large eddy simulation on flame topologies and the blow-off characteristics of ammonia/air flame in a model gas turbine combustor. *Fuel* **2021**, *298*, 120846. [CrossRef]
35. Wu, X.; Wang, H.; Wei, D.; Shi, M. ANFIS with natural language processing and gray relational analysis based cloud computing framework for real time energy efficient resource allocation. *Comput. Commun.* **2020**, *150*, 122–130. [CrossRef]
36. Hayakawa, A.; Arakawa, Y.; Mimoto, R.; Somarathne, K.D.K.A.; Kudo, T.; Kobayashi, H. Experimental investigation of stabilization and emission characteristics of ammonia/air premixed flames in a swirl combustor. *Int. J. Hydrogen Energy* **2017**, *42*, 14010–14018. [CrossRef]
37. Zhao, X.; Yang, W.; Chong, C.T.; Chai, W.S.; Poon, H.M.; Wang, W.; Valera-Medina, A.; Chiong, M. NH_3/CH_4 and NH_3/Biogas swirl combustion: Turbulent flame propagation and sensitivity analysis of NO emissions. *Energy Fuels* **2025**, *39*, 11325–11338. [CrossRef]
38. Yang, W.; Zhao, X.; Xian, S.; Mong, G.R.; Ooi, J.B.; Wong, K.Y.; Lim, W.H.; Wang, W.; Chiong, M. Thermo-scalar flame structure and NH_2 radical chemistry in NH_3/CH_4 and NH_3/Biogas swirl combustion. *Int. J. Hydrogen Energy* **2026**, *201*, 152997. [CrossRef]
39. Wang, Z.; Liu, W.; Xu, H.; Xia, Y.; Sun, J.; Dong, M.; Liu, H.; Yao, S. Stability and NO formation of swirling CH_4/NH_3 co-combustion flames under controlled mixing strategies. *Int. J. Hydrogen Energy* **2026**, *261*, 156690. [CrossRef]
40. Durox, D.; Moeck, J.P.; Bourgouin, J.; Morenton, P.; Viallon, M.; Schuller, T.; Candel, S. Flame dynamics of a variable swirl number system and instability control. *Combust. Flame* **2013**, *160*, 1729–1742. [CrossRef]
41. Innocenti, A.; Andreini, A.; Bertini, D.; Facchini, B.; Motta, M. Turbulent flow-field effects in a hybrid CFD-CRN model for the prediction of NOx and CO emissions in aero-engine combustors. *Fuel* **2018**, *215*, 853–864. [CrossRef]
42. Xiao, H.; Valera-Medina, A.; Marsh, R.; Bowen, P.J. Numerical study assessing various ammonia/methane reaction models for use under gas turbine conditions. *Fuel* **2017**, *196*, 344–351. [CrossRef]
43. Savarese, M.; Procacci, A.; Iavarone, S.; Giuntini, L.; Paepe, W.D.; Parente, A. A sparse sensing and Chemical Reactor Network based framework for the development of physics-based digital twins of combustion devices. *Proc. Combust. Inst.* **2024**, *40*, 105536. [CrossRef]
44. Wu, X.; Wang, H.; Tan, W.; Wei, D.; Shi, M. Dynamic allocation strategy of VM resources with fuzzy transfer learning method. *Peer Peer Netw. Appl.* **2020**, *13*, 2201–2213. [CrossRef]
45. Okafor, E.C.; Naito, Y.; Colson, S.; Ichikawa, A.; Kudo, T.; Hayakawa, A.; Kobayashi, H. Measurement and modelling of the laminar burning velocity of methane-ammonia-air flames at high pressures using a reduced reaction mechanism. *Combust. Flame* **2019**, *204*, 162–175. [CrossRef]
46. Okafor, E.C.; Naito, Y.; Colson, S.; Ichikawa, A.; Kudo, T.; Hayakawa, A.; Kobayashi, H. Experimental and numerical study of the laminar burning velocity of CH_4–NH_3–air premixed flames. *Combust. Flame* **2018**, *187*, 185–198. [CrossRef]
47. Mao, L.; Wang, P.; Shrotriya, P.; He, H.; Ferrante, A. Laminar flame speed and NO emission characteristics of premixed flames with different ammonia containing fuels. *CIESC J.* **2021**, *72*, 5330–5343.
48. Stagni, A.; Cavallotti, C.; Arunthanayothin, S.; Song, Y.; Herbinet, O.; Battin-Leclerc, F.; Faravelli, T. An experimental, theoretical and kinetic-modeling study of the gas-phase oxidation of ammonia. *React. Chem. Eng.* **2020**, *5*, 696–711. [CrossRef]
49. Zhang, K.; Luo, T.; Li, Y.; Zhang, T.; Li, X.; Zhang, Z.; Shang, S.; Zhou, Y.; Zhang, C.; Chen, X.; et al. Effect of ignition, initial pressure and temperature on the lower flammability limit of hydrogen/air mixture. *Int. J. Hydrogen Energy* **2022**, *47*, 15107–15119. [CrossRef]
50. Mikofski, M.A.; Williams, T.C.; Shaddix, C.R.; Blevins, L.G. Flame height measurement of laminar inverse diffusion flames. *Combust. Flame* **2006**, *146*, 63–72. [CrossRef]
51. Hayakawa, A.; Goto, T.; Mimoto, R.; Arakawa, Y.; Kudo, T.; Kobayashi, H. Laminar burning velocity and Markstein length of ammonia/air premixed flames at various pressures. *Fuel* **2015**, *159*, 98–106. [CrossRef]
52. Zhang, M.; An, Z.; Wei, X.; Wang, J.; Huang, Z.; Tan, H. Emission analysis of the CH_4/NH_3/air co-firing fuels in a model combustor. *Fuel* **2021**, *291*, 120135. [CrossRef]
53. An, Z.; Zhang, M.; Zhang, W.; Mao, R.; Wei, X.; Wang, J.; Huang, Z.; Tan, H. Emission prediction and analysis on CH_4/NH_3/air swirl flames with LES-FGM method. *Fuel* **2021**, *304*, 121370. [CrossRef]
54. Ku, J.W.; Ahn, Y.J.; Kim, H.K.; Kim, Y.H.; Kwon, O.C. Propagation and emissions of premixed methane-ammonia/air flames. *Energy* **2020**, *201*, 117632. [CrossRef]
55. Lindstedt, R.P.; Lockwood, F.C.; Selim, M.A. Detailed Kinetic Modelling of chemistry and temperature effects on ammonia oxidation. *Combust. Sci. Technol.* **1994**, *99*, 253–276. [CrossRef]
56. Mikulčić, H.; Baleta, J.; Wang, X.; Wang, J.; Qi, F.; Wang, F. Numerical simulation of ammonia/methane/air combustion using reduced chemical kinetics models. *Int. J. Hydrogen Energy* **2021**, *46*, 23548–23563. [CrossRef]
57. *GB/T 10180—2017*; Test Procedures for Thermal Performance of Industrial Boilers. AQSIQ: Beijing, China, 2018.
58. Genichiro, N.; Hiroki, I.; Takamasa, I.; Emi, O.; Yoshitomo, O. Development of co-firing method of pulverized coal and ammonia to reduce greenhouse gas emissions. *IHI Eng. Rev.* **2020**, *53*, 1–10.

59. Nozari, H.; Karaca, G.; Tuncer, O.; Karabeyoglu, A. Porous medium based burner for efficient and clean combustion of ammonia–hydrogen–air systems. *Int. J. Hydrogen Energy* **2017**, *42*, 14775–14785. [CrossRef]
60. Yapicioglu, A.; Dincer, I. Experimental investigation and evaluation of using ammonia and gasoline fuel blends for power generators. *Appl. Therm. Eng.* **2019**, *154*, 1–8. [CrossRef]
61. *DB44/765-2019*; "Emission Standard of Air Pollutants for Boilers" (Guangdong Province). Guangdong Provincial Academy of Environmental Sciences: Guangzhou, China, 2019; Volume 2026.
62. Mashruk, S.; Okafor, E.C.; Kovaleva, M.; Alnasif, A.; Pugh, D.; Hayakawa, A.; Valera-Medina, A. Evolution of N_2O production at lean combustion condition in NH_3/H_2/air premixed swirling flames. *Combust. Flame* **2022**, *244*, 112299. [CrossRef]
63. Li, Q.; Ma, L.; Zhou, J.; Li, J.; Yan, F.; Du, J.; Wang, Y. A comprehensive parametric study on NO and N_2O formation in ammonia-methane cofired premixed flames: Spatially resolved measurements and kinetic analysis. *Combust. Flame* **2025**, *272*, 113851. [CrossRef]

Disclaimer/Publisher's Note: The statements, opinions and data contained in all publications are solely those of the individual author(s) and contributor(s) and not of MDPI and/or the editor(s). MDPI and/or the editor(s) disclaim responsibility for any injury to people or property resulting from any ideas, methods, instructions or products referred to in the content.